IEEE Access
Multidisciplinary | Rapid Review | Open Access Journal

Received August 31, 2016, accepted October 25, 2016, date of publication November 7, 2016, date of current version January 27, 2017.

Digital Object Identifier 10.1109/ACCESS.2016.2626200

Predicting Atmospheric Attenuation Under Pristine Conditions Between 0.1 and 100 THz

JINGYE SUN, (Student Member, IEEE), FANGJING HU, (Member, IEEE), AND STEPAN LUCYSZYN, (Fellow, IEEE)

Centre for Terahertz Science and Engineering, Department of Electrical and Electronic Engineering, Imperial College London, London, SW7 2AZ, U.K.

Corresponding author: S. Lucyszyn (s.lucyszyn@imperial.ac.uk)

This work was supported in part by Imperial College MRC Confidence in Concept (ICiC) fund and NIHR Imperial BRC funding 2015/16.

ABSTRACT This multidisciplinary paper reports on a research application-led study for predicting atmospheric attenuation, and tries to bridge the knowledge gap between applied engineering and atmospheric sciences. As a useful comparative baseline, this paper focuses specifically on atmospheric attenuation under pristine conditions, over the extended terahertz spectrum. Three well-known simulation software packages ('HITRAN on the Web', MODTRAN®4, and LBLRTM) are compared and contrasted. Techniques used for modeling atmospheric attenuation have been applied to investigate the resilience of (ultra-)wide fractional bandwidth applications to the effects of molecular absorption. Two extreme modeling scenarios are investigated: horizontal path links at sea level and Earth-space path links. It is shown by example that a basic software package ('HITRAN on the Web') can give good predictions with the former, whereas sophisticated simulation software (LBLRTM) is required for the latter. Finally, with molecular emission included, carrier-to-noise ratio fade margins can be calculated for the effects of line broadening due to changes in macroscopic atmospheric conditions with sub-1-THz ultra-narrow fractional bandwidth applications. Outdoors can be far from pristine, with additional atmospheric contributions only briefly introduced here; further discussion is beyond the scope of this paper, but relevant references have been cited.

INDEX TERMS THz, thermal infrared, atmospheric attenuation, transmittance, carrier-to-noise, molecular absorption, molecular emission, HITRAN, MODTRAN®, LBLRTM, THz Torch.

I. INTRODUCTION

Indoor terahertz (THz) laboratories routinely conduct experiments on optical benches within an atmosphere under pristine conditions. For example, in an air-conditioned environment, sometime even without humidity control; or without the recommended vacuum or inert gas. Alternatively, compressed dry air can be employed to avoid the risk of asphyxiation (a possible danger when using an inert gas like nitrogen or argon), although oxygen absorption lines will remain. Measurement discrepancies due to adverse effects from atmospheric attenuation may not always be properly taken into account.

With another scenario, the relentless drive to push future (ultra-)broadband systems up into the THz spectrum require ever-more sophisticated channel modeling (taking into account additional aspects; for example, non-line-of-sight paths and multipath fading). Once again, atmospheric attenuation is important; in this case it represents a critical contribution to the free-space power link budget analysis used to predict the system's end-to-end carrier-to-noise ratio. Therefore, an understanding of atmospheric attenuation, how it can be predicted and its quantifiable effects on systems level performance is important. This multidisciplinary paper tries to bridge the knowledge gap between applied engineering and atmospheric sciences; and is intended for non-atmospheric researchers interested in predicting atmospheric attenuation.

As a useful comparative baseline, this paper focuses specifically on atmospheric attenuation under pristine conditions (found indoors and some global location outdoors), within the extended terahertz spectrum. From the outset, an exhaustive review of simulation software and their associated theoretical background and validation is beyond the scope of this study. More realistic modeling scenarios would require a much broader and deeper treatment of atmospheric sciences, including a very detailed be-spoke (time-variant) atmospheric model across the geographical path link under investigation.

Nevertheless, our idealized treatment reveals many important facets associated with this multidisciplinary subject.

When referring to 'terahertz' it is useful to first define associated frequency bands. Often, 'terahertz' is loosely defined by the broad frequency range from 0.1 to 10 THz. This region is sometimes referred to as the *"THz Gap"*, where the performance of conventional electronic(photonic) devices fall off with increasing frequency(wavelength). Over time, this technology gap continues to shrink; leading to the International Telecommunications Union (ITU)-designated spectral range from 0.3 to 3 THz (also known as the submillimeter-wave band). With reference to heterodyne receivers, frequencies >3 THz are sometimes referred to as ''super-THz'' [1]. For optics and photonics, the International Organization for Standardization quote the far infrared (FIR) as being from 0.3 to 6 THz and mid-infrared (MIR) from 6 to 100 THz [2]. When dealing with Earth systems, Harries *et al.* [3] defines the FIR as THz frequencies below 20 THz; while in spectroscopy, the FIR extends from 0.3 to 30 THz and MIR from 30 to 120 THz [4]. Here, the spectroscopic definitions for the infrared are adopted and the *'over the THz horizon'* thermal infrared from 10 to 100 THz is considered as an extension of the THz spectrum. To illustrate the spectral locations for various key bands, Planck's law for spectral radiance of a blackbody radiator at room temperature (e.g., 296 K or 23°C) as a function of frequency is plotted over the extended THz spectrum from 0.1 to 100 THz, shown in Fig. 1.

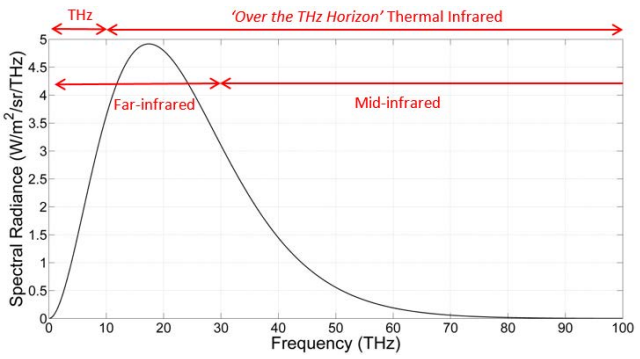

FIGURE 1. Calculated Planckian spectrum for a blackbody radiator at 296 K as a function of frequency. (Spectral bands defined here are overlaid in red).

For a blackbody radiator, the theoretical peak in spectral radiance is given by Wien's displacement law; for example, at 296 K the emitted spectral radiance as a function of frequency peaks at 17.4 THz. However, the Planckian spectral tail theoretically extends down in frequency towards dc. This explains why thermal detectors can still operate at microwave frequencies.

One of the inherent limiting factors for practical free-space THz applications (such as spectroscopy, sensing, imaging, communications and wireless power transfer) is atmospheric attenuation. This has a strong influence on the power link budget of complete end-to-end systems and ultimately limits its dynamic range and maximum path length. As a result, accurately predicting atmospheric attenuation is of critical importance for experimentalists and systems designers.

Three well-known simulation software packages ('HITRAN on the Web', MODTRAN®4 and LBLRTM) are compared and contrasted for predicting atmospheric attenuation from 0.75 to 100 THz. It will be shown that atmospheric attenuation is relatively very low if path lengths are of the order of centimeters, or tens of meters within certain bands. This offers many new opportunities for potentially ubiquitous free-space applications in spectroscopy (e.g., non-destructive testing), sensing (e.g., motion detection, radiometry, radar), imaging, communications (e.g., key fobs, smart RFID, high data rate terrestrial, drone and satellite links) and radiative wireless power transfer (R-WPT).

Section II gives a background to the characterization of atmospheric attenuation within the far and mid-infrared parts of the electromagnetic spectrum. The paper then investigates, by examples, two very different idealized scenarios (i.e., under pristine atmospheric conditions, which ignores aerosols and mist/fog/cloud/precipitation). In Sections III and IV, horizontal path links at sea level (i.e., 1 atm or 101.325 kPa) are investigated, using the three well-known simulation software packages. In Section V, Earth-space path links are investigated using the gold standard reference benchmark software (LBLRTM). Finally, Section VI investigates sub-1THz scenarios.

II. BACKGROUND

Atmospheric attenuation includes contributions from three generic categories: (i) gases; (ii) aerosols; and (iii) mist/fog/cloud/precipitation. These are represented respectively by either molecules, particles or liquid droplets; all of which may absorb and scatter radiation with a frequency dependence that is a function of their size, shape and composition. A knowledge of atomic and molecular physics can explain and quantify how various gaseous molecules absorb radiation at specific frequencies, as well as the formation of 'transmission windows'.

Natural aerosols include forest exudates, pollen, mineral dust and wildfire smoke; while anthropogenic aerosols include industrial haze, dust, as well as smoke, and particulate air pollutants.

In addition to absorption, specular (mirror-type) and diffuse (random) reflections can occur. An example of the former is tropospheric scattering found at low gigahertz frequencies, and longer wavelengths, and thus below our spectral range of interest. With the latter, the amount of scattering depends on the levels of concentration, size, shape and composition (represented by its refractive index) of the scatterer.

All scattering effects are ultimately governed by Maxwell's equations and dependent on the size parameter x (equal to the ratio of physical peripheral size of scatterer to excitation wavelength). As can be seen in Fig. 2, there are four scattering regimes: (i) no scattering with $x < 0.002$; (ii) Rayleigh (or molecular) scattering with $0.002 < x < 0.2$; (iii) Mie

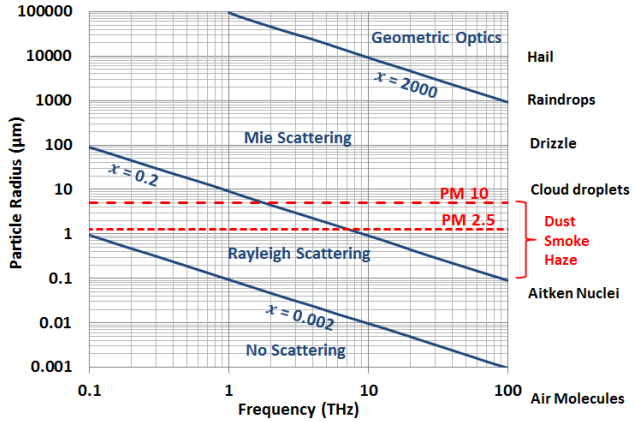

FIGURE 2. Scattering regimes that influence diffuse reflections.

scattering with $0.2 < x < 2000$; and (iv) geometric optics with $x > 2000$ [5]. This idealized treatment makes the implicit assumption that the particles or liquid droplets are spherical, which is a generalized approximation.

Within our spectral range of interest, a combination of Rayleigh scattering, Mie scattering and geometric optics can occur from aerosols and mist/fog/cloud/precipitation, as the size of the particles or liquid droplets increases.

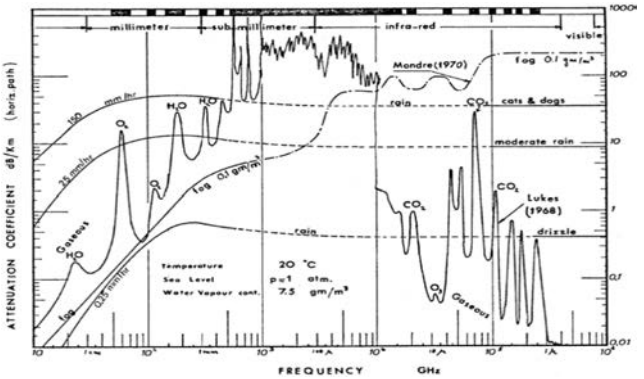

FIGURE 3. Early (1972) piecemeal modeling approach representation of atmospheric attenuation for horizontal path links at sea level for different weather conditions, reproduced in [6].

Atmospheric attenuation from microwave to visible frequencies is represented in Fig. 3, for different weather conditions [6]. It can be seen that the effects of gaseous water vapor dominates atmospheric attenuation from *ca.* 0.6 to 10 THz, while rain can have an influence at all frequencies. As with aerosols, fog causes little attenuation at low THz frequencies, when compared at shorter wavelengths. The level of atmospheric attenuation by precipitation depends on rainfall rate, and the size and distribution of droplets.

It is interesting to note that Fig. 3 was re-published within the past decade [6], but a search for the original artwork revealed numerous variations [7]. For gaseous attenuation, they state that results below 1 THz were published by Rosenblum in 1961 [8] and above 10 THz by Lukes in 1968 [9]. However, between 1 and 10 THz, these authors conceded that this region was drawn-in by hand [6]. The results for fog between 0.01 to 1,000 THz are from Mondre in 1970 [10]. Finally, data for atmospheric attenuation due to rain, below 0.6 THz, was from Zufferey in 1972 [11] and above 0.6 THz from Lukes [9]. While the results shown in Fig. 3 give qualitative spectral information, it should not be used to extract accurate quantitative data values; not least because the results only serve for specific scenarios (temperature, pressure, rainfall rate, etc.).

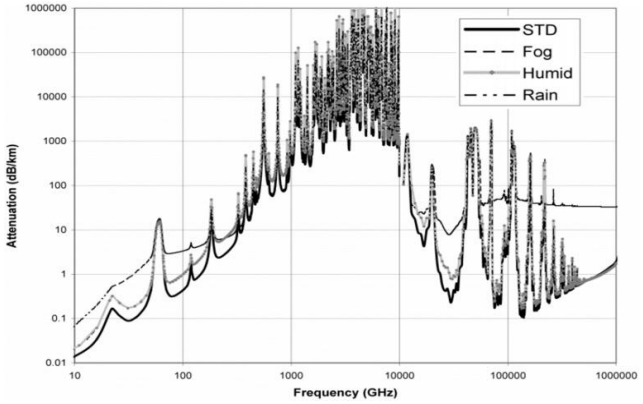

FIGURE 4. Atmospheric attenuation for horizontal path links at sea level for different weather conditions [6].

In the highly cited papers by Appleby and Wallace [6] and Rosker and Wallace [12] atmospheric attenuation is simulated between 0.01 and 1,000 THz, shown in Fig. 4, using three atmospheric radiative transfer codes – from 0.01 to 1 THz with MPM89 [13]; 1 to 10 THz with FASCODE [14] and LBLRTM [15]; and 10 to 1,000 THz with MODTRAN®4 (released in 1999) [16], [17] – for a horizontal path link at sea level, given various weather conditions. It can be seen in Fig. 4 that the relative coverage, spectral resolution and agreement at the overlap points indicate the improved ability to model atmospheric attenuation across this spectral range. Nevertheless, because of poor print quality, it is still generally not possible to directly extract data from plots in published papers from 1 to 10 THz. In practice, atmospheric attenuation should be predicted using simulation software having a be-spoke model for the specific link scenario under investigation.

For example, a typical modeling scenario for radio astronomy requires the prediction of transmittance through the Earth's atmosphere at zenith. In 2013, Shaw and Nugent [18] reported results above 14 THz, from sea level to the top of atmosphere (i.e., vertical path through the atmosphere), using the MODTRAN®5 Rural aerosol model with 23 km visibility; the result is shown in Fig. 5.

It is important to note that, within today's atmospheric science communities, atmospheric attenuation modeling is a very advanced and highly specialized discipline. For example, extensive theoretical and experimental work has been undertaken to characterize the effect of gaseous water vapor on atmospheric attenuation within the 0.1 to 10 THz region [19]–[24] and above 10 THz [25]–[27].

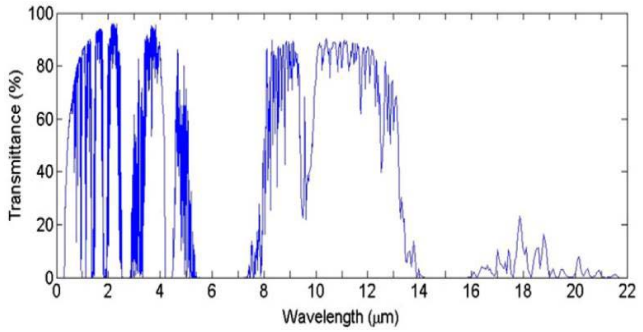

FIGURE 5. Atmospheric transmittance for Earth-space path links at zenith using the U.S. standard 1976 model with MODTRAN®5 [18].

Atmospheric attenuation measurements conducted within a controlled atmosphere was reported by Liu *et al.* [23], covering the 0.1 to 3 THz frequency range, at a temperature of 296 K and relative humidity of 26%. It was found that there are 9 transmission windows within this spectral range and that, as expected, transmittance decreases with an increase in relative humidity; while transmission windows shrink as path lengths increase.

Recently, Slocum *et al.* [24] reported the transmittance between 0.3 to 1.5 THz for multiple humidity levels and path lengths, using Fourier transform spectroscopy. They compared the modeled absorption lines of gaseous water vapor with experimental data from a controlled environment. A discrepancy was observed due to water vapor continuum absorption and the air-broadening continuum parameter was determined. This mechanism will be discussed further in Section III.

In 2008, an international collaborative study (by Imperial College London, CNR, Universities of Bologna and Basilicata and NASA Langley Research Centre) modeled atmospheric attenuation from dc to 30 THz [3]. More recently, within the pure rotation band, between 2.5 and 12.5 THz, measurements were taken using the Imperial College London Tropospheric Airborne Fourier Transform Spectrometer (TAFTS) instrument on-board the Facility for Airborne Atmospheric Measurement (FAAM) BAe-146 research aircraft [28].

Accurately predicting atmospheric attenuation should be possible for any arbitrarily defined geographical path link and at any frequency. However, developing generic in-house software for this purpose is challenging, because of the ever-expanding database of spectral features and choice of parameters used in subsequent calculations. For this reason, well-established benchmark simulation software has been developed for the scientific and engineering communities. These codes are constantly being updated to take into account recent advances in experimental atmospheric spectroscopy.

Using such software, Schneider *et al.* [29] investigated the influences of different weather conditions (including fog, cloud and rain) on propagation from 1 GHz to 1 THz. Here, atmospheric attenuation was predicted using three ITU-Recommendations [30]–[32] and the *am* simulation software package [33]. The ITU-R P.676 models have been adopted as an industry standard for predicting atmospheric attenuation (due to oxygen and water vapor molecular absorption) between 1 GHz and 1 THz, with values that can even be extracted directly from plots. Developed by the Harvard-Smithsonian Center for Astrophysics, *am* performs radiative transfer calculations from microwave to submillimeter-wave frequencies. Five transmission windows were identified, shown in Table 1, for data transmission over a fixed free-space path length of 1 km, between 0.3 and 0.9 THz; under pristine conditions, 50 m visibility fog and worst-case rainfall rates of 50 mm/h.

TABLE 1. Sub-1 THz free-space transmission windows for horizontal path links at sea level.

Schneider *et al.* 2012 [29] †			Akyildiz *et al.* 2014 [37] ‡		
Designation	Central frequency (GHz)	Bandwidth (GHz)	Designation	Cut-off frequencies (GHz)	Bandwidth (GHz)
w_1	338	76	-	-	-
w_2	414	58	w_1	380 - 440	60
w_3	484	62	w_2	450 - 520	70
w_4	669	85	w_3	620 - 720	100
w_5	855	94	w_4	770 - 920	150

† Cut-off frequencies defined for worst-case atmospheric attenuation below 100 dB/km with 50 mm/h rainfall rate over a 1 km path length.
‡ Cut-off frequencies defined for worst-case atmospheric attenuation of 10 dB/km under pristine conditions over a 10 m path length.

A path loss analysis (which combines both atmospheric attenuation and spreading loss) for channel modeling between 0.1 and 10 THz was reported by Jornet and Akyildiz [34]. Analysis is based on radiative transfer theory [35] and data from the HITRAN database [36] above 1 THz in their calculations of atmospheric attenuation due to molecular absorption. The total loss for path lengths from 10 μm to 10 m have been calculated for gaseous water vapor fractional volumes of 0.1% and 10%. They then reported total path losses under pristine conditions for 1, 10 and 100 m path lengths [37]. From their recent study, they independently proposed four transmission windows between 0.1 and 1 THz, shown in Table 1.

In their recently published paper [38], the same group investigated the relationship between the distance and the total usable bandwidth for wireless systems, within the spectral range from 0.06 to 1 THz for line-of-sight (LOS) and multipath (MP) propagation models. With the former, and the use of highly directional pencil-beam antennas, the range of communications is limited to 70 m with a 120 dB threshold path loss; the usable bandwidth shrinks from 0.94 to 0.26 THz when path length increases from 1 to 70 m. With the latter, path links are limited to 8 m with a lower threshold path loss of 80 dB; the usable bandwidth is now 0.29 THz at a path length of 1 m.

III. COMPARISON OF SELECTED SIMULATION SOFTWARE

There are two important differences between the results shown in Figs. 4 and 5. The first is that attenuation is replaced by transmittance; with the latter being a more useful way of viewing atmospheric absorption/emission lines and bands.

At a single frequency point, attenuation has a linear scaling law with path length; while transmittance has a power law. However, over a band of frequencies, the mean band attenuation(transmittance) can only exhibit a linear(power) scaling law relationship if its values are effectively constant across the band. In practice, this scenario is only likely to exist over narrow bandwidths. Secondly, results for the horizontal path link at sea level will be different to that for the Earth-space path link at zenith, given the same path length of ∼100 km, due to the variation in absorber (gases, aerosols and mist/fog/cloud/precipitation) concentration levels and macroscopic atmospheric conditions (e.g., temperature and pressure) with altitude. Gaseous water vapor variation is particularly important, as it plays the dominant role between *ca.* 0.1 and 10 THz.

In this section, three well-known simulation software packages will be compared and contrasted. Before doing this, some of the most relevant output parameters are first defined from first principles.

When an electromagnetic wave is incident upon a non-opaque medium (solid, liquid or gas), some of this power P_i is reflected back P_r, a proportion may be absorbed P_a and the remaining transmitted through P_t; such that the principle of conservation of energy is observed at each frequency (i.e., $P_i = P_r + P_a + P_t$) [39]. In terms of absolute power values, benchmark simulation software can generate results for: (i) reflection or reflectance, $R = P_r/P_i$; (ii) absorptivity, absorption or absorptance, $A = P_a/P_i$; and (iii) transmission or transmittance, $T = P_t/P_i = \mathrm{e}^{-\tau}$, where $\mathrm{e}^{+\tau}$ is the atmospheric loss factor, $\tau = \gamma L$ is the opacity, $\gamma = (b + k_\alpha)$ is the extinction coefficient, b is the scattering coefficient, k_α is the attenuation or absorption coefficient and L is path length. Apart from path length, all other variables are implicitly frequency dependent.

The gradient of attenuation with path length can be expressed (in dB/km) as specific attenuation $= -10log_{10}\{T\} = -10log_{10}\{1 - R - A\}$, where *R, T, A* have been calculated for a specific reference path length (e.g., $L_{REF} = 1$ km); an example of this is shown in Fig. 4. Therefore, at a single frequency point, attenuation (dB) over an arbitrary path length L (km) within a homogeneous atmosphere can be calculated from $-L \cdot 10log_{10}\{T\} = -L \cdot 10log_{10}\{1 - R - A\}$, which exhibits a linear scaling law. Similarly, transmittance (%) over L can be calculated from $T^{L/L_{REF}} \cdot 100\%$; exhibiting a power law. Both of these relationships are only true if the atmosphere is homogeneous (such that $\gamma \neq f(l)$, where l is the location along the path).

To represent realistic vertical atmospheric profiles, radiative transfer codes typically split the atmosphere into a number of sub-layers. Given N homogeneous sub-layers, each having different gaseous concentrations and macroscopic atmospheric conditions, the monochromatic transmittance of the whole atmosphere will be $T = \prod_{i=1}^{N} e^{-\gamma_i L_i}$; hence neither linear nor power scaling laws are valid.

As a useful comparative baseline, only pristine conditions are considered further. Here, molecular scattering from gas species is only significant at visible frequencies (outside our spectral range of interest) and so scattering and, therefore, diffuse reflections can be ignored.

Every gas has its own unique absorptance and transmittance spectra, composed of discrete absorption/emission lines, which can cluster into bands. Each line is centered at a specific frequency, having an associated width and depth of absorption. The spectral location and shape of each discrete line is dependent on the molecule's quantum-mechanical properties, as well as the macroscopic atmospheric conditions [40]. For gas mixtures, the superposition of absorption lines for each gas has to be calculated. HITRAN [36] is perhaps the most comprehensive and commonly used database for characterizing gaseous absorption lines, giving molecular spectroscopic information (e.g., transition line center and intensity, and also air- and self-broadening half-widths) that is used as input to various radiative transfer codes. This line parameter database information, combined with atmospheric models are used by a variety of benchmark simulation software, with the selection of frequency range, resolution, etc., to predict atmospheric attenuation, as illustrated in Fig. 6.

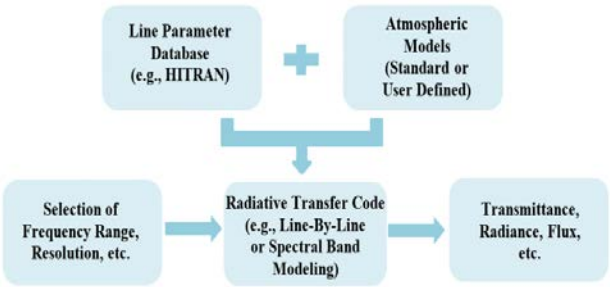

FIGURE 6. Illustration showing the generic process within atmospheric benchmark simulation software.

In experimental studies of infrared absorption from gaseous water vapor, it is found that there is a significant 'broad-band' excess of absorption occurring. This can be observed as a broader spectral feature, having a gradual roll-off in the transmission window, and cannot be explained by theoretical spectral line absorption. This residual absorption is known as 'water vapor continuum absorption' and consists of two contributions: self-continuum (or 'wet continuum' [41]), due to the interaction between water vapor molecules; and foreign-continuum (or 'dry continuum'), due to the interaction of water vapor molecules with other atmospheric gas molecules (normally nitrogen and oxygen).

It is believed that the self-continuum contribution is due to the superposition of far reaching spectral wings from strong gaseous water vapor spectral lines in neighboring absorption bands [42]. This hypothesis is strongly supported by the experimental results of Bignell *et al.* [43]. However, it has also been proposed that this is caused by pairs of water vapor molecules being loosely bound by hydrogen bonds (i.e., water dimers) [44], [45]. The cause and mechanisms that are responsible for self-continuum absorption remain an active area of scientific research.

Absorption due to foreign-continuum is much weaker than self-continuum absorption between 25 and 37.5 THz (12 and 8 μm). Therefore, it is difficult to take accurate absorption measurements within this spectral region. As a result, the contribution of foreign-continuum absorption is either considered to be negligible [25], [46] or underestimated in radiative transfer calculations. Fortunately, the water vapor self-continuum and foreign-continuum absorption phenomena have been modeled using a semi-empirical approach; namely the Mlawer-Tobin-Clough-Kneizys-Davies (MT_CKD) model [47], which is generally used by most radiative transfer codes in climate modeling, numerical weather prediction and remote sensing of the Earth. Even below 1 THz, water vapor continuum absorption has been characterized [48], [49].

With a real atmosphere, an absorption/emission line will have some finite width, due to line-broadening effects that result from collisions between molecules (pressure or Lorentz broadening) and the velocity of the molecules (Doppler or Gaussian broadening). At higher pressures (e.g., above 0.1 atm or 10 kPa) the Lorentz line shape dominates; while the Gaussian line shape dominates at lower pressures (e.g., below 0.01 atm or 1 kPa). The Voigt line shape is the convolution of the Lorentz and Gaussian broadening mechanisms, and is most commonly used because it gives a reasonable fit to the observed behavior over the full range of atmospheric conditions.

The broadening of lines means that some choice has to be made as to the spectral range to be considered when modeling the extent of their wings (sometimes expressed in terms of the number of line half-widths to include). This choice of spectral line wing length is also important because the spectral range of interest may have strong contributions from absorption lines that lie outside this region, which need to be accounted for. For this reason, wing length is set here to the highest possible value, at the expense of increased computation time. Finally, the apparatus function emulates the measurement system's frequency-domain sampling aperture. For maximum spectral resolution, 'no influence of the device' should be selected.

There are more than 30 different radiative transfer codes available; three popular molecular absorption databases are also available (HITRAN, JPL and GEISA) [50], [51]. The following subsections will compare and contrast three well-known simulation software packages – 'HITRAN on the Web' [52], MODTRAN® and LBLRTM – for transmittance under the same conditions of: (i) horizontal path links at sea level with path lengths of 1 mm (reactive near field probing scale), 1 m (standoff detection distance) and 1 km (communications range); (ii) HITRAN database; (iii) macroscopic atmospheric conditions (i.e., 296 K and 101.325 kPa); and (iv) NASA's U.S. standard 1976 model [53] for mid-latitude, to represent a homogeneous atmosphere (given in Table 2), modified from its original temperature of 288.15 K (15°C) and gas species fractional volumes.

TABLE 2. NASA's U.S. standard 1976 model at sea level [53] modified for gas species and temperature of 296 K.

Gas Species	Fractional Volume (%)
Nitrogen (N_2)	78.084
Oxygen (O_2)	20.9
Water vapor (H_2O)	0.7745
Carbon dioxide (CO_2)	0.033
Methan (CH_4)	0.00017
Nitrous oxide (N_2O)	0.000032
Carbon monoxide (CO)	0.000015
Ozone (O_3)	0.00000266

A number of atmospheric trace gases and inert gases are not fully included in Table 2. This includes anthropogenic source contributions of pollutant gases, such as carbon monoxide (CO), nitrogen dioxide (NO_2), sulfur dioxide (SO_2) and ammonia (NH_3). Indeed, from vehicular emissions, carbon monoxide reacts with other pollutants in the air to increase levels of tropospheric greenhouse gases such as ozone (O_3), carbon dioxide (CO_2) and methane (CH_4). The Russian standard uses its Institute of Atmospheric Optics model, which includes small traces of SO_2 and NH_3; not significant within our spectral range of interest. The inert gases are radiatively inactive, since they do not possess either an electric or magnetic dipole moment, and so do not absorb infrared radiation. Nitrogen is not truly inert, and so included here, as it exhibits vibrational transitions and continuum absorption in the extended THz spectrum at ~71 THz.

Some software (e.g., 'HITRAN on the Web') assumes a homogeneous atmosphere, and thus ignores specular reflections, while others (e.g., MODTRAN® and LBLRTM) can split-up the atmosphere into discrete homogeneous sub-layers. Moreover, with software that only considers pristine conditions and ignores molecular scattering (e.g., 'HITRAN on the Web'), diffuse reflections are ignored. Therefore, when no reflectance data is generated, attenuation results are deflated, as they are calculated directly from either A or $T = 1 - A$ (with both A and T being inflated).

The research-led motivation for our work is the need to accurately predict atmospheric attenuation for incoherent thermal infrared channels; more specifically, the mean channel transmittance against path length for thermal infrared '*THz Torch*' applications [54]–[60]. To this end, the following software simulation tools were investigated.

A. HITRAN ON THE WEB (HotW)

The HITRAN (HIgh-resolution TRANsmission) database [36], [61] was created by the U.S. Air Force Cambridge Research Laboratories (AFCRL) in the early 1970s and later the Atomic and Molecular Physics Division, Harvard-Smithsonian Centre for Astrophysics, contributed by updating its database. Its spectroscopic parameters are often revised by improved experimental techniques, measurements

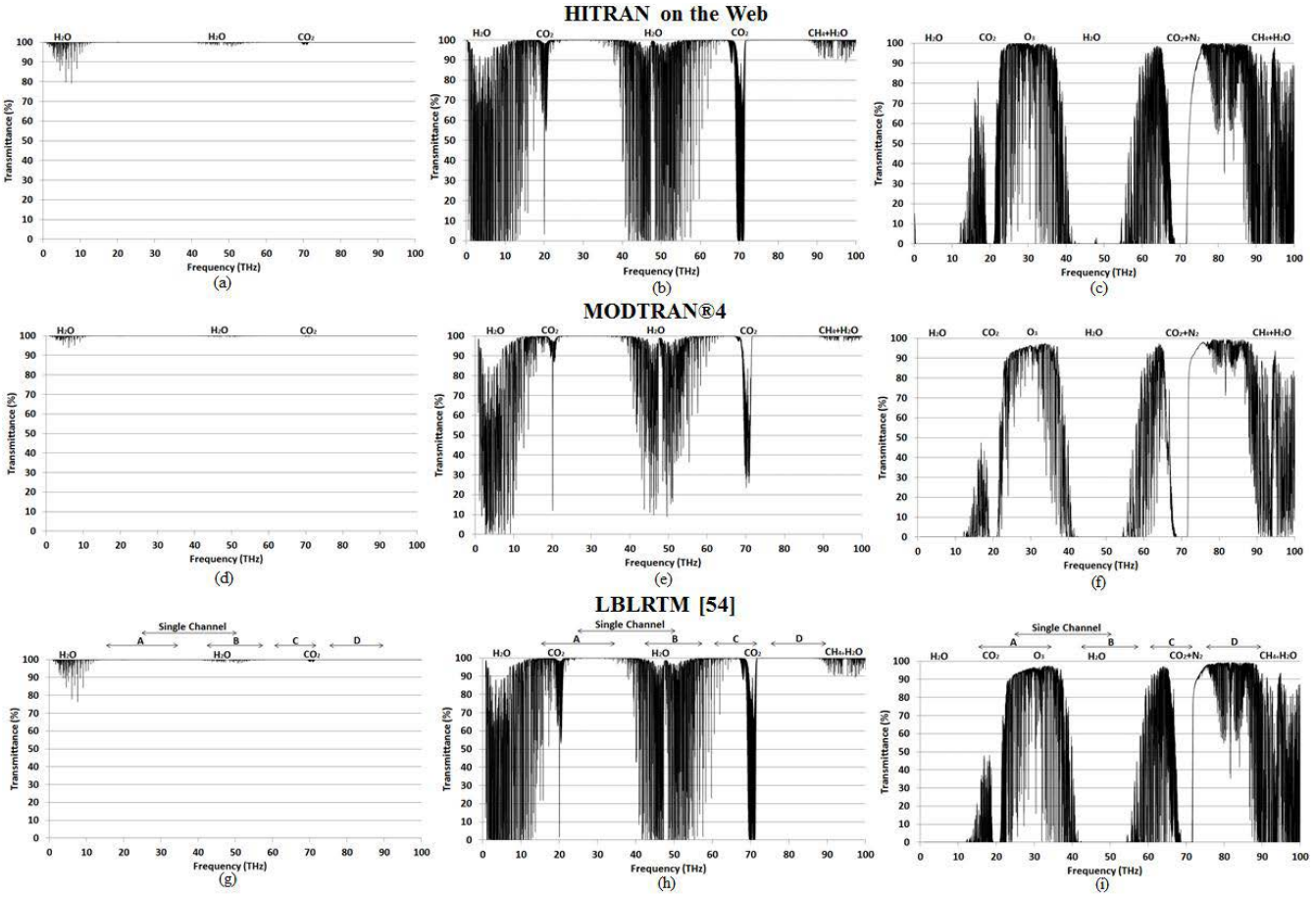

FIGURE 7. **Predicted transmittance against frequency for horizontal path links at sea level using the modified U.S. standard 1976 model (at 296 K) for mid-latitude with different path lengths: 'HITRAN on the Web' for (a) 1 mm; (b) 1 m; and (c) 1 km; MODTRAN®4 for (d) 1 mm; (e) 1 m; and (f) 1 km; and LBLRTM for (g) 1 mm; (h) 1 m; and (i) 1 km. (Channel allocations for thermal infrared *'THz Torch'* proof-of-concept demonstrators are overlaid).**

and analysis; with a maximum spectral resolution of 30 kHz (wavenumber of 0.000001 cm^{-1}).

'HITRAN on the Web' [52] is jointly supported by the U.S. Civic Research and Development Foundation (CRDF) and the Russian Foundation for Basic Research (RFBR). It uses high resolution spectral line-by-line methods, based on the Beer-Lambert law to calculate the spectral radiance (or intensity) ratio of incident level received to radiated level emitted (equivalent to transmittance). The software is designed to provide information about spectral line parameters for natural and pollutant gases. 'HITRAN on the Web' has the important advantages of unrestricted access, a very simple user-interface, and is free to use. Different gas mixture models can be selected; a be-spoke atmospheric model can also be created for registered users. Additional user settings are listed in Table 3, along with parameter values used in our simulations.

'HITRAN on the Web' can display molecular absorption lines (e.g., through absorption coefficient, absorption and transmittance spectra). In addition, radiances originating from molecular emission at a given temperature can also be calculated and displayed. Planck's law for spectral radiance as a function of wavenumber I_{BB} is weighted by the emissivity ε at each wavenumber, such that the emitted spectral radiance is $I = \varepsilon \cdot I_{BB}$. Under thermodynamic equilibrium, $\varepsilon = A$. Hence, since absorptivity is a function of physical parameters (e.g., path length, temperature and pressure) and I_{BB} is a function of wavenumber and temperature, the emitted spectral radiance is also dependent on these parameters.

TABLE 3. **'HITRAN on the Web' user settings and parameter values.**

Parameter	Value	Units
Minimum wavenumber, WN_{min}	3.33	cm^{-1}
Maximum wavenumber, WN_{max}	3333.33	cm^{-1}
Temperature, T	296	K
Pressure, P	1	atm
Intensity cut-off, I_{cut}	10^{-28}	cm/mol
Line shapes, *Shape*	Voigt	–
Wavenumber step, WN_{step}	0.01	cm^{-1}
Spectral line wing length, *Wing*	1000	half-width
Optical path length, *Opt. path*	0.001 to 1000	m
Apparatus function, *AF*	no influence of the device	–

Figure 7(a)-(c) shows predicted transmittances from 0.1 to 100 THz, with a spectral resolution of 0.3 GHz

(corresponding to $WN_{step} = 0.01$ cm^{-1}). The atmospheric contribution of gaseous water vapor can be seen in Fig. 7(a)-(c) over short and long path lengths, at frequencies less than 20 THz (due to pure molecular rotations) and within the mid-infrared from 42 to 57 THz. A partially transparent window, in the 12 to 18 THz region, is due to the lower intensity levels of the gaseous water vapor transitions. The effect of carbon dioxide can be seen from 18 to 21.6 THz (due to molecular vibrations) and at ∼70 THz; becoming more pronounced as path length increases. The results are consistent with those reported by Brindley and Harries [62]. In the 25 to 37.5 THz region, the extinction coefficient of CO_2 is only ∼0.02 km^{-1}, which is small when compared to the total value of 0.15 km^{-1} [25]. Hence, in this region, water vapour is more dominant than CO_2. The influence of ozone at ∼31 THz is relatively insignificant with the horizontal path link at sea level, but methane and gaseous water vapor have some effects over longer path lengths between 90 and 100 THz. The contributions from other molecular species (due to pure rotational transitions or low-energy vibrational transitions) in this region are insignificant when compared to those from gaseous water vapor and carbon dioxide.

It should be noted that gaseous water vapor and carbon dioxide continuum absorptions are not considered by 'HITRAN on the Web'. Nevertheless, 'HITRAN on the Web' is a useful tool for investigating spectral lines. Since it does not include continuum absorption for predicting atmospheric attenuation it can only qualitatively show the broader spectral features of the transmission window. For horizontal path links, 'HITRAN on the Web' can still be used to good effect for predicting mean band transmittance for (ultra-)wide fractional bandwidth applications (seen in Section IV) and demonstrating line broadening (seen in Section VI).

B. MODTRAN®4

MODTRAN® (MODerate resolution atmospheric TRANsmission) [63] is an atmospheric radiative transfer code, developed since 1987 by Spectral Sciences Inc. and the U.S. Air Force Research Laboratory. This software has a more sophisticated process than 'HITRAN on the Web'.

It can incorporate the effects of gases, aerosols and mist/fog/cloud/precipitation absorption and emission, as well as scattering, while its spectral range extends from the far-infrared to the ultraviolet. However, even the latest version, MODTRAN®6 [64], has a maximum spectral bin resolution of 3 GHz (0.1 cm^{-1}). In essence, MODTRAN® employs a spectral band approach that implicitly makes approximations for mean band transmittance based on the underlying spectroscopy. With this new version, released in 2016, the algorithm solves the line-by-line radiative transfer equations at arbitrarily fine spectral resolution within the 0.1 cm^{-1} spectral bins.

While not considered here, this software has a number of different aerosol models, which include rural, urban and maritime [65]. The rural model has 70% water-soluble material (e.g., ammonium, calcium sulphate and organic compounds) and 30% dust-like aerosols. The urban model has 80% of the rural aerosols, mixed with 20% carbonaceous aerosols (to represent anthropogenic contributions). The maritime model has a sea-salt component and a continental component (rural model that excludes the larger dust-like particles).

Significant differences between simulation results obtained from 'HITRAN on the Web' and MODTRAN® are to be expected, due to the available spectral resolution and water vapor continuum absorption. For our work, MODTRAN®4 was used [16], [17]. Figure 7(d)-(f) shows predicted transmittances from 0.75 to 100 THz, with its maximum spectral resolution of 30 GHz (1 cm^{-1}).

Due to the representation of continuum absorption, the mathematical formulation used in MODTRAN®4 should only scan a range of ±0.75 THz (±25 cm^{-1}) for either side of a given line or band. Hence, the lowest recommended frequency that MODTRAN® should go down to is 0.75 THz.

When compared to Fig. 7(c), it can be seen between 25 and 37.5 THz in Fig. 7(f) that the transmission window roll-off is due to water vapor continuum absorption. Therefore, 'HITRAN on the Web' has better spectral resolution, while MODTRAN® is more accurate at showing broader spectral features.

C. LBLRTM

LBLRTM (Line-By-Line Radiative Transfer Model) emerged in the 1980s from the Fast Atmospheric Signature Code (FASCODE) program. LBLRTM was originally developed by the U.S. Air Force Research Laboratory and now by the Atmospheric and Environmental Research's Radiative Transfer Working Group. Its spectral range extends from the submillimeter wave frequency range to the ultraviolet. The main features of LBLRTM are described by Clough *et al.* [66].

LBLRTM combines the spectral resolution advantage of 'HITRAN on the Web' with the accurate broader spectral features associated with MODTRAN®. LBLRTM has: (i) arbitrarily fine spectral resolution; (ii) incorporates both self- and foreign-broadened water vapor continuum absorption models; (iii) additional continua for carbon dioxide, oxygen, nitrogen, ozone; and (iv) extinction due to Rayleigh scattering.

This software extracts gaseous absorption line parameters from the HITRAN database (e.g., half-width temperature dependence, pressure shift coefficient and coefficient for the self-broadening of gaseous water vapor), as well as from other databases. Similar to 'HITRAN on the Web', the Voigt line shape is used with an algorithm that linearly combines line approximation functions. In general, limiting errors are due to those associated with the line parameters and shapes (given in the line parameter database), since errors associated with computations are five orders of magnitude

less than those associated with the line parameters [67]. For these reasons, LBLRTM is considered by some as the gold standard reference benchmark atmospheric modeling software, used in radiative transfer applications (such as retrieving information on temperature, water vapor and trace gas concentrations) [67], [68].

As with MODTRAN®4, mathematical formulation limits the lowest recommended frequency of LBLRTM to 0.75 THz. Figure 7(g)-(i) shows predicted transmittances from 0.75 to 100 THz, with a spectral resolution of 0.3 GHz (0.01 cm^{-1}). As seen with shorter path lengths, the lower transmittance predicted is due to the two orders of magnitude improvement in resolution when compared with MODTRAN®4. With longer path lengths, as with MODTRAN®4, the noticeable low-frequency roll-off in transmittance below 37.5 THz is due to water vapor continuum absorption.

IV. MEAN BAND TRANSMITTANCE FOR EXTENDED TERAHERTZ SPECTRUM APPLICATIONS

The extended terahertz spectrum from 0.1 to 100 THz can find many scientific, military and commercial free-space applications. Examples include THz time-domain spectroscopy (THz-TDS) [69]–[71], infrared spectroscopy (time and frequency domains) [72], radiometry and limb sounding [73]–[75], thermography [76], communications [54]–[57], [60] with ∼30 THz R-WPT [77], to mention just a few. An example of broadband THz-TDS has been developed by the Japanese National Institute of Information and Communications Technology (NICT), having a spectral coverage from 0.1 to 15 THz [71]. The atmospheric THz-TDS measurements at NICT were performed within a vacuum-tight enclosure at room temperature, having an atmospheric path length of 80 cm [71]. The chamber was first purged with nitrogen gas, to act as a reference; this was followed by measuring the transmission spectrum for air. The system is based on NICT's photoconductive antennas that can operate over this ultra-wide spectral range [78]–[81].

The thermal infrared *'THz Torch'* concept was first introduced by Lucyszyn *et al.* in 2011, for short-range secure communications over a single (25 to 50 THz) channel [55]. It fundamentally exploits engineered blackbody radiation, by partitioning thermally-generated spectral power into predefined frequency channels; the incoherent signal power within each channel is then independently pulsed modulated. More recently, advances in the foundations [56], [58], [60], subsystems level analysis [54], and multichannel communications [57] and spectroscopy [59] applications have been reported; incorporating frequency band multiplexing techniques across the 15 to 89 THz range. The single-channel (defined by the 70% transmittance cut-off frequencies) and multichannel (with Channels A, B, C and D defined by the 50% transmittance cut-off frequencies) *'THz Torch'* demonstrator frequency ranges are given in Table 4.

In general, applications may have frequency channels with ultra-narrow (≲0.1%) or narrow (≲10%) fractional bandwidths located between discrete absorption/emission lines; while others may spread across wide (≳20%) or ultra-wide (≳50%) fractional bandwidths, 'seeing' many discrete lines and/or strong bands. With (ultra-)wideband systems, it is important to be able to accurately calculate the mean band transmittance. This will determine the level of resilience of free-space systems to atmospheric absorption/emission; particularly with ultra-broad band coherent applications such as THz-TDS and incoherent applications that include radiometry-based remote sensing and thermal infrared *'THz Torch'* systems. This latter application is considered further. Multichannel *'THz Torch'* communications acts as a suitable exemplar for the quantitative prediction of mean channel transmittance under pristine conditions with a horizontal path link at sea level, at an ambient temperature of 296 K.

TABLE 4. Mean channel transmittance for horizontal path links at sea level (at 296 K) over a 1 cm path length

Channel Frequency (THz)	Mean Channel Transmittance					
	HITRAN		MODTRAN®4		LBLRTM	
	(%)	dB	(%)	dB	(%)	dB
Single Channel						
25-50	99.82	0.0078	99.59	0.0177	99.82	0.0080
Multiple Channel						
A : 15-34	99.99	0.0005	99.98	0.0007	99.99	0.0005
B : 42-57	99.59	0.0177	99.07	0.0406	99.58	0.0184
C : 60-72	99.81	0.0082	99.81	0.0083	99.81	0.0084
D : 75-89	100	0.0000	100	0.0000	100	0.0000

There are two different approaches for calculating mean channel transmittance. The first simply uses the statistical mean; while the second takes the ratio of incident radiance at the input of a receiver to radiated radiance from a blackbody emitter. A detailed discussion on the merits for both is given in Appendix A. While the latter is more accurate (adopted here), it will be seen in Appendix A that the simpler approach can still be used in certain circumstances.

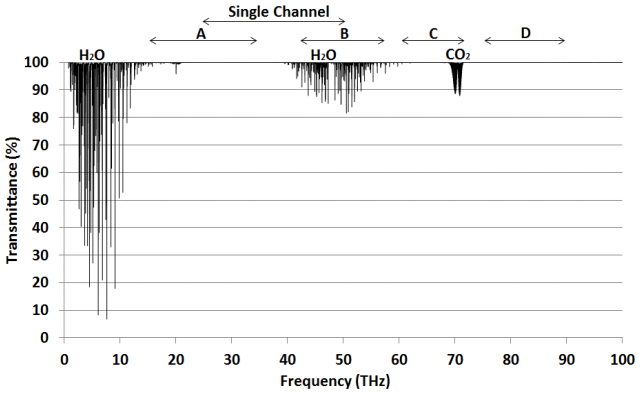

FIGURE 8. Predicted transmittance against frequency using LBLRTM for horizontal path links at sea level using the modified U.S. standard 1976 model (at 296 K) over a 1 cm path length. (Channel frequencies for *'THz Torch'* proof-of-concept demonstrators are overlaid).

The channel frequencies used in early thermal infrared *'THz Torch'* proof-of-concept demonstrators, having a 1 cm

path length, are overlaid onto the LBLRTM predicted transmittance results shown in Fig. 8. The mean channel transmittance for Channel B 'sees' the effects of gaseous water vapor, while part of Channel C 'sees' the effects of carbon dioxide. The quantitative mean channel transmittance (%) and corresponding attenuation (dB) for all the channels are given in Table 4. As expected, Channel B has the lowest mean channel transmittance, although still >99%. This quantitatively proves that atmospheric attenuation is not a fundamental limitation within this spectral range for very short-range (ultra-)broad bandwidth applications. Table 4 also includes the comparative results from using 'HITRAN on the Web' and MODTRAN®4, indicating no significant variation in results between software packages over such a short path length.

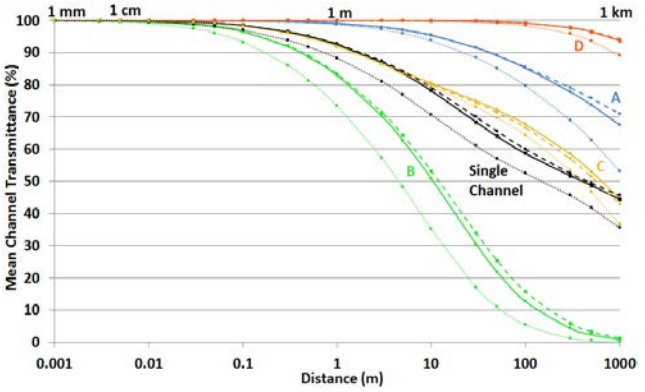

FIGURE 9. Calculated mean channel transmittance against horizontal path length (at sea level) for different *'THz Torch'* channels, using predictions from 'HITRAN on the Web' (dashed), MODTRAN®4 (dotted) and LBLRTM (solid) at 296 K and 101.325 kPa.

The mean channel transmittance against path length for horizontal paths links at sea level is shown in Fig. 9, using the three different software packages. With Channels A and B, 'HITRAN on the Web' predicts larger values than MODTRAN®4 and LBLRTM, because water vapor continuum absorption is not taken into account. The influence of gaseous water vapor on Channel B with path length is evident; mean channel transmittance is only 0.2% at 1 km (i.e., 27 dB/km). Channel C shows sensitivity to carbon dioxide. Channel D has the highest mean channel transmittance, because its passband matches that of a transmission window; being ∼93% at 1 km (i.e., 0.3 dB/km). For a worst-case mean channel transmittance of 50%, it can be seen that the multichannel thermal infrared *'THz Torch'* systems can potentially operate up to a path length of 10 m; while increasing the Channel B transmit power (as compensation for its greater atmospheric attenuation) can extend this range even further. Alternatively, if only Channel D is used then the single-channel system can operate up to and beyond 1 km; opening up the technology for new medium range applications – for example, noise radio [82], noise radar [83], [84], thermal infrared camouflage and identification, friend or foe (IFF) [85].

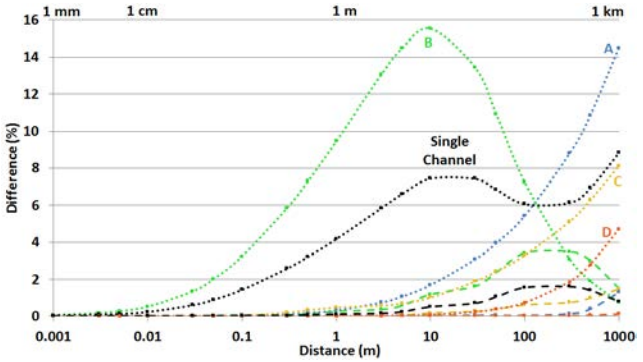

FIGURE 10. Deviation in calculated transmittance data from LBLRTM with 'HITRAN on the Web' (dashed) and MODTRAN®4 (dotted) seen in Fig. 9.

Fig. 10 shows the deviation in transmittance for 'HITRAN on the Web' and MODTRAN®4, using LBLRTM as our gold standard reference benchmark software. While both MODTRAN®4 and LBLRTM take into account water vapor continuum absorption, the different spectral resolutions result in greater differences when compared with 'HITRAN on the Web' and LBLRTM. The latter pair of simulation software have the same spectral resolution and use line-by-line methods. Fig. 10 shows the water vapor continuum absorption influence is less significant than the difference in spectral resolution; this is particularly evident with Channels A and B. It can be concluded that the free and easy to use (even by a non-atmospheric scientists) 'HITRAN on the Web' software can give good predictions of mean channel transmittance for (ultra-)wide fractional bandwidth applications.

The relationship between mean band transmittance, frequency and fractional bandwidth for any horizontal path link at sea level, under pristine conditions, between 0.75 and 100 THz is shown in Fig. 11, calculated using predictions from LBLRTM for a 1 km path length. This color map can act as a useful tool for channel spectral allocation.

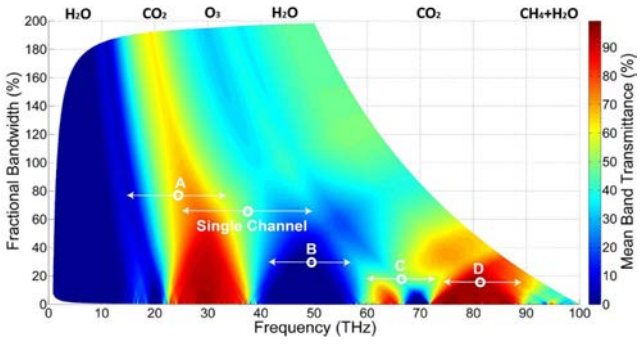

FIGURE 11. Calculated color map of mean band transmittance against frequency and fractional bandwidth for horizontal path links at sea level, using predictions from LBLRTM at 296 K over a 1 km path length.

As an example, the thermal infrared *'THz Torch'* channel characteristics are superimposed onto Fig. 11. For each channel, the color representation of mean channel transmittance at the center of the white circle corresponds to the value

in Fig. 9 for the 1 km path length. Given a fixed center frequency, the performance of Channel B can be improved by increasing its fractional bandwidth. Alternatively, for a fixed fractional bandwidth, improvement can be achieved by translating its original ∼50 THz center frequency either towards 40 or 60 THz.

V. EARTH-SPACE PATH LINK SIMULATIONS

In this Section, the effects of atmospheric attenuation on Earth-space path links will be investigated, using LBLRTM for pristine atmospheric conditions, from 0.75 to 100 THz. Thru-atmosphere transmittance is calculated for both (ultra-)wide (with incoherent source radiation) and ultra-narrow (with coherent source radiation) fractional bandwidth applications.

The top of atmosphere (TOA) is considered to be ∼100 km (the Karman line defines this geometric altitude for the boundary between the Earth's atmosphere and outer space). In terms of the Earth's geometric altitude, the lowest three atmospheric layers are the troposphere (0-10 km), stratosphere (10-50 km) and mesosphere (50-86 km).

In addition, Earth-space path links include propagation through the ionosphere (50-1,000 km), which experiences attenuation (from absorption and diffusion), refraction, depolarization (Faraday rotation) and propagation delay variations [86]. However, since ionization (caused by solar radiation) has an associated plasma frequency of $\sim 9\sqrt{electron\ density} \leq 9$ MHz for a typical maximum electron density of 10^{12} electrons/m^3 within the ionospheric 'F2' region (at an altitude of ∼280 km), ionospheric effects are insignificant above 2 GHz [86] and so not considered further.

A. RADIO ASTRONOMY

In the case of radio astronomy (operating over the extended THz spectrum), where telescopes are located in regions having low levels of natural and anthropogenic aerosols, atmospheric attenuation is dependent exclusively on atmospheric precipitable water vapor (PWV). This represents the total water content in a column of the atmosphere, from sea level to the TOA, represented by liquid water [87]. The influence of gaseous water vapor can be mitigated by locating ground stations in regions having drier climates.

Recent work by Suen *et al.* [87], analyzed the global PWV distributions over the entire Earth's surface using high-resolution data from two NASA Earth Observing System (EOS) satellites: Aqua and Terra. Using MODTRAN®5 they produced transmittance spectra for Earth-space path links at zenith from dc to 1.6 THz, for values of PWV from 0 to 20 mm [87]. They also then compared their MODTRAN®5 transmittance spectra with results from *am*. It was found that MODTRAN®5 and *am* give almost identical results with values of PWV = 0.5 mm. However, with PWV = 0, *am* predicts a near linear drop-off in transmittance with frequency, not seen in the MODTRAN®5 spectrum. The authors suggested that this is because dry air collision-induced absorption is not modeled in MODTRAN®5.

TABLE 5. Transmission windows for terabit-per-second satellite links [89].

Designation	Cut-off frequencies (GHz)	Central frequency (GHz)	Bandwidth (GHz)	Transmitter power density (W per 3 GHz bandwidth)
Band A	66 - 186	n/a	120	3
Band B	186 - 327	225	141	1.25
Band C	327 - 555	350	228	0.175
Band D	567 - 747	675	180	0.1
Band E	759 - 984	875	225	0.05
Band F	996 - 1086	1025	90	0.01

The same researchers identified several dry locations, such as Chile (where the international Atacama Large Millimeter/Submillimeter Array (ALMA) is located, having Band 10 operating from 0.787 to 0.950 THz [88]), Antarctica, Greenland Ice Sheet, Tibetan Plateau and high peaks in the Western United States [87]. A more extreme solution would be to locate infrared radiometers in space (with the Herschel Space Observatory, operating from 0.48 to 5.3 THz, being a good example).

B. SATELLITE COMMUNICATIONS

The same research group, from the University of California, Santa Barbara, modeled ground-to-geostationary satellite links at frequencies from 0.066 to 1.1 THz. The THz spectrum is segmented into 6 bands, shown in Table 5. It has been suggested that, even with severe atmospheric attenuation, Tbit/s Earth-space links are possible [89], since the satellite link only experiences atmospheric attenuation from an equivalent path length of several kilometers from a dry location at sea level. As an example, with 45° elevation, for a low Earth orbit (LEO) link (780 km altitude) and a geostationary equatorial orbit (GEO) link (35,768 km altitude), the equivalent ground path length is less than 10 km in the THz windows [90].

C. GROUND-BASED RECEIVER LOCATED AT GIZA

Giza (30.0° N, 31.1° E, in Egypt) was chosen as an arbitrary location at sea level, having very low levels of gaseous water vapor. As illustrated in Fig. 12, an ambient temperature T_{AS} = 296 K (at sea level) and zenith angle of 33° are considered. The following analysis will show the importance of modeling the Earth's atmosphere when calculating transmittance and carrier-to-noise ratio at the input to a ground-based receiver.

A 2012 annual mean dataset was taken from the nearest location to Giza (at 30.0° N, 31.5° E), based on an atmospheric reanalysis dataset (a combination of measurement observations and modeling), considered as the current state of the art [91]. This provides realistic vertical profiles for gaseous water vapor and ozone, as well as many other parameters.

For Giza, our assumption of pristine conditions can in theory represent a reasonable approximation. At this

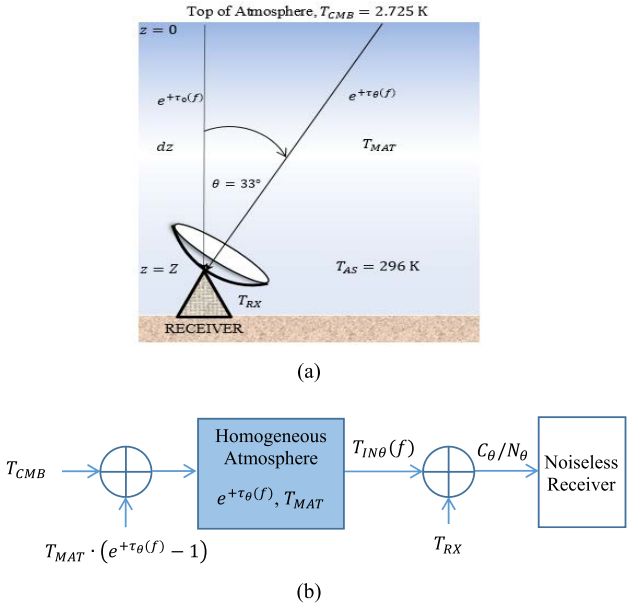

FIGURE 12. **(a) Ground-based receiver located at Giza (30.0° N, 31.1° E) with 33° zenith angle. (b) Simplified equivalent noise model for a homogeneous atmosphere.**

location, with some of the minor gases (e.g., CO_2, CH_4 and N_2O), fractional volumes for the (near-)vertical path links are different to those given in Table 2. In addition, relevant chlorofluorocarbons (CFCs) have also been included; not considered with the U.S. standard 1976 model used with the previous horizontal path links at sea level. In practice, Giza is at times affected by the presence of aerosols (in the form of large mineral dust particles), which typically absorb and scatter within the thermal infrared [92].

For predicting atmospheric attenuation, a realistic barometric pressure against atmospheric temperature profile was created from the reanalysis dataset (the barometric pressure is then divided into 46 sub-layers). The geopotential altitude against atmospheric temperature profile can then be calculated (with atmospheric temperature having a near-linear relationship within each of the 46 sub-layers of geopotential altitude). More details are given in Appendix B.

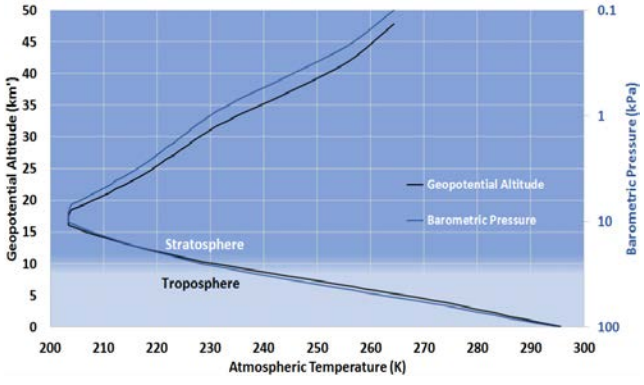

FIGURE 13. **Atmospheric temperature profile against geopotential altitude (black) and barometric pressure (blue) for our (near-)vertical LBLRTM simulations within the troposphere and stratosphere for a sea-level temperature of 296 K.**

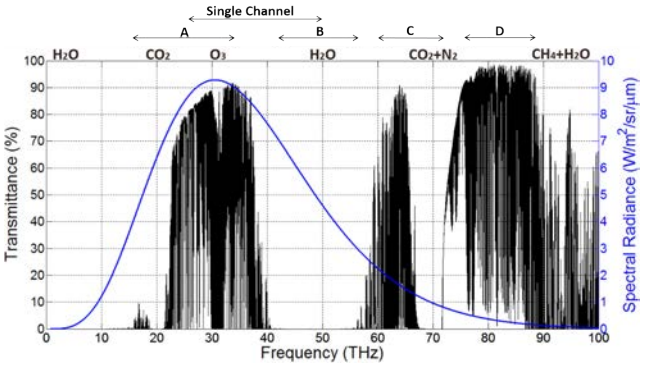

FIGURE 14. **Predicted Earth-space path link transmittance for the ground-based receiver located at Giza with 33° zenith angle using LBLRTM (black) and calculated Planckian spectrum for a blackbody radiator at 296 K as a function of wavelength (blue).**

The results for both barometric pressure and geopotential altitude against atmospheric temperature are shown in Fig. 13. These plots only extend to a barometric pressure of 0.1 kPa (found at a geopotential altitude of 47.64 km′), as it only has 0.11% of the standard sea-level atmospheric gas density [53]. Therefore, since the concentration of air molecules is so low, their effects at higher geopotential altitudes become insignificant (even though the TOA is at ∼100 km). It can be seen from Fig. 13 that barometric pressure is logarithmically related to geopotential altitude. More importantly, while the localized sea-level temperature is fixed at 296 K, microscopic atmospheric conditions (temperature and pressure) varies significantly with geopotential altitude.

For high accuracy, a spectral resolution of 0.3 GHz was used by LBLRTM to predict the Earth-space path link transmittance, using the barometric pressure against atmospheric temperature profile shown in Fig. 13 at a zenith angle of 33°, with predictions given in Fig. 14. The Planckian spectrum for a blackbody radiator at 296 K as a function of wavelength (plotted against frequency) is also shown in Fig. 14. From Wien's displacement law, the emitted spectral radiance as a function of wavelength has a peak at 9.8 μm (30.6 THz).

From Fig. 14, it can be seen that there are three main transmission windows through the Earth's atmosphere, between 0.75 and 100 THz – with thru-atmosphere 50% transmittance cut-off frequencies of 22.6 & 38.2 THz, 59.1 & 65.9 THz and 72.4 & 90.0 THz. The effect of absorption by the ozone layer (having a maximum concentration within the stratosphere at around 25 km) is found at ∼31 THz and not evident in horizontal path links at sea level.

It is interesting to compare the results from this location and macroscopic atmospheric conditions with those from Harries *et al.* [3]; demonstrating the benefits of operating under pristine conditions at zenith with a subarctic winter standard and from a geometric altitude of 8 km. With this extremely dry, cold and elevated altitude, transmittance between 24 to 29 THz is approximately 100%, compared to <88% shown in Fig. 14. This extreme condition can also be exploited by long-haul aircraft, for establishing terabit per second satellite links, while maintaining a cruising altitude

TABLE 6. Mean channel transmittance for ground-based receiver located at Giza having 0° and 33° zenith angles.

Channel Frequency (THz)	Fractional Bandwidth (%)	Mean Channel Transmittance 0 degree (%)	0 degree dB	33 degree (%)	33 degree dB
Single Channel					
25-50	66.7	33.18	4.7907	31.42	5.0279
Multiple Channel					
A : 15-34	77.6	50.51	2.9664	47.84	3.2019
B : 42-57	30.3	0.09	30.6070	0.05	33.2745
C : 60-72	18.2	26.80	5.7190	24.23	6.1572
D : 75-89	17.1	82.96	0.8115	80.68	0.9326

above *ca*. 10 km to avoid the bulk contribution of atmospheric attenuation found at lower altitudes.

D. (ULTRA-)WIDE FRACTIONAL BANDWIDTH (≳20%) CHANNELS

This subsection considers the scenario shown in Fig. 12, with the (ultra-)wide fractional bandwidth thermal infrared *'THz Torch'* application, introduced in Section IV. The quantitative mean channel transmittance (%) and corresponding attenuation (dB) from LBLRTM predicted data for both 0° and 33° zenith angles are given in Table 5.

It can be seen in Table 5 that mean channel transmittance degrades with zenith angle, due to the longer thru-atmosphere path length. However, this is only an increase of 0.24 dB for the single channel case, having a 66.7% fractional bandwidth. Moreover, at 33°, the mean channel transmittance of 5 dB demonstrates resilience to spectral absorption by the many discrete absorption lines between 25 and 38 THz and the strong absorption band between 38 and 50 THz for the single channel case.

In principle, if large emitting areas and narrow collimated beams are implemented, Channels A, C and D could be used in Earth-space path links; for example, communications between ground stations and 1U CubeSats (having geometric altitudes above 200 km), the International Space Station (maintaining an geometric altitude from 330 to 435 km) or highly elliptical orbit satellites (with an geometric altitude at perigee above 500 km). For some applications, however, high atmospheric absorption can be exploited. For example, local-area networks, drone-to-drone communications and inter-satellite links can mitigate against interference, interception and jamming.

E. ULTRA-NARROW FRACTIONAL BANDWIDTH (≲0.1%) CHANNELS

This subsection also considers the scenario shown in Fig. 12, with ultra-narrow fractional bandwidth applications. A close-in view of the peak in transmittance within the lowest of the three transmission windows (in Fig. 14), found between *ca.* 33.8 to 33.9 THz, is shown in Fig. 15.

It can be seen that transmittance is approximately 90% (or 0.46 dB) across this 100 GHz bandwidth. With ultra-narrow fractional bandwidth applications that use coherent source radiation, channels should ideally avoid spectral absorption lines. Be-spoke channel frequencies would then have 50% transmittance bandwidths that range between 3 and 22 GHz.

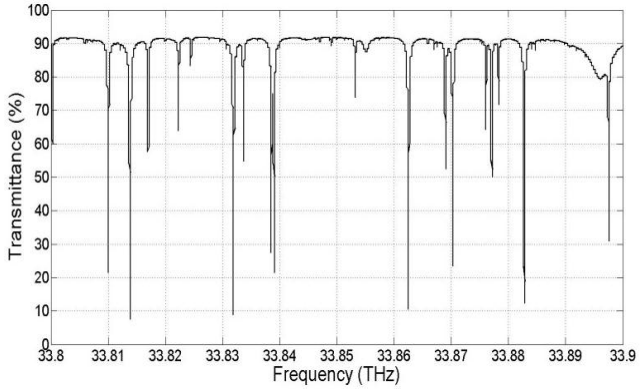

FIGURE 15. Predicted Earth-space path transmittance, from 33.8 to 33.9 THz, for the ground-based receiver located at Giza with 33° zenith angle using LBLRTM.

Within the (at present) unregulated thermal infrared, large and freely available channel bandwidths offer new opportunities for both coherent and (even more so) incoherent radiation applications. The former can take advantage of the increasingly popular room temperature mid-infrared quantum cascade laser sources [93] for low power applications. While high power CO_2 lasers, operating between 26 and 33 THz, can be used for long range communications and R-WPT applications.

With the latter, it is interesting to compare the peak in transmittance at 33.9 THz (8.8 μm) with the peak in spectral radiance as a function of wavelength corresponding to a frequency of 30.6 THz (9.8 μm) for a blackbody radiator at 296 K. Unsurprisingly, thermography represents a ubiquitous application for incoherent source radiation at these frequencies (e.g., infrared thermometers, thermal infrared motion sensors, thermal cameras); in nature, pit viper snakes and vampire bats have evolved to exploit the lowest transmission window (in Fig. 14) to 'visually' locate thermally-contrasting warm-blooded pray.

VI. SUB-1 THz ANALYSIS

A. SOFTWARE PREDICTIONS AND ITU-R P.676-10 ESTIMATIONS FOR HORIZONTAL PATH LINKS AT SEA LEVEL

It has previously been stated that MODTRAN® and LBLTRM are designed for use from far-infrared and submillimeter-wave frequencies, respectively, to the ultraviolet. Moreover, both employ the HITRAN database. However, neither of these simulation software packages nor 'HITRAN on the web' are used at the lower end of our spectral range of interest. Instead, line-by-line calculations are adopted, defined by the ITU-R P.676 model for frequencies below 1 THz, as reported by Schneider *et al.* [29].

It is, therefore, of interest to investigate how well our three software packages compare with ITU-R P.676-10 [94] estimates for frequencies below 1 THz. This published

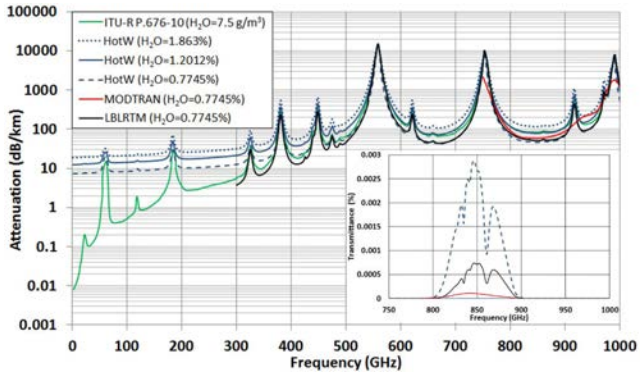

FIGURE 16. Predicted specific attenuation for horizontal path links at sea level using simulation software packages and calculated estimates from ITU-R P.676-10 at 288.15 K.

recommendation is based on a gaseous water vapor density of 7.5 g/m^3, at a temperature of 288.15 K (15°C) and at 1 atm, with results plotted in Fig. 16. While LBLTRM and MODTRAN® are recommended for use above 0.75 THz, predictions can still be given above 0.3 THz for LBLRTM, as show in Fig. 16. It can be seen that the predictions from LBLRTM and MODTRAN®4 follow the estimates from ITU-R P.676-10, but are not accurate. This is due to ITU-R P.676-10 having a different gaseous water vapor fractional volume to the modified U.S. standard 1976 model for mid-latitude [53] used here by LBLRTM and MODTRAN®4. This is also true for 'HITRAN on the Web', which can make spectral predictions down to dc. With this software package, while all spectral lines for oxygen and gaseous water vapor are evident, the predictions only follow the ITU-R P.676-10 estimates down to *ca.* 0.38 THz. As frequency decreases below *ca.* 0.38 THz, predictions become increasingly erroneous; results from 'HITRAN on the Web' converge on a specific attenuation value of 10 dB/km at dc.

Note that the default atmospheric model for 'HITRAN on the Web' is the summer U.S.A. model for mean latitude at sea level, having a 1.862987% gaseous water vapor fractional volume [52]. This level of fractional volume predicts excess atmospheric attenuation. However, from the modified U.S. standard 1976 and summer U.S.A. models, if the geometric mean value of 1.2012% is adopted for the gaseous water vapor fractional volumes, 'HITRAN on the Web' predictions are very close to the ITU-R P.676-10 estimates down to *ca.* 0.56 THz. The inset of Fig. 16 shows almost negligible transmittance, with a minimum specific attenuation of 50 dB/km from 0.75 to 1 THz, even with the conservative values for the modified U.S. standard 1976 model.

B. HORIZONTAL PATH LINKS AT DIFFERENT ALTITUDES

This subsection highlights the sensitivity of line broadening due to extreme changes in macroscopic atmospheric conditions, as geopotential altitude increases. For horizontal path links, Table 7 gives the macroscopic atmospheric conditions extracted directly from the U.S. standard 1976 model for mid-latitude [53].

TABLE 7. Macroscopic atmospheric conditions at different altitudes for horizontal path links using the U.S. standard 1976 model [53]

Barometric Pressure (kPa)	Barometric Pressure (atm)	Geopotential Altitude (km')	Atmospheric Temperature (K)	Relative Gas Density (%)
0.101325	0.001	47.64	270.65	0.107
1.01325	0.01	30.95	227.6	1.27
10.1325	0.1	16.06	216.65	13.38
101.325	1	0	288.15	100

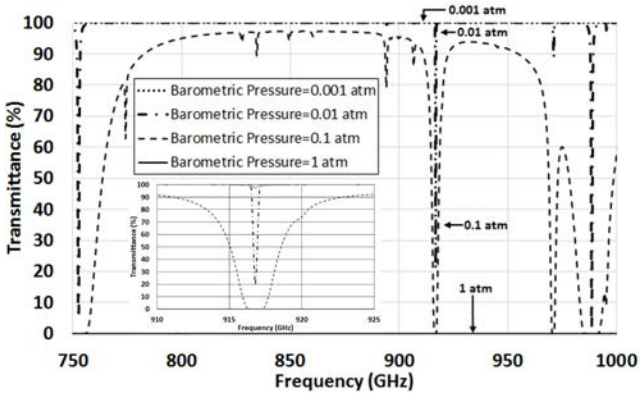

FIGURE 17. Predicted transmittance using 'HITRAN on the Web' for 1 km horizontal path links at different geopotential altitudes using the modified U.S. standard 1976 model.

For convenience, 'HITRAN on the Web' is used to predict transmittance, as it gives similar results to LBLRTM (as seen in Fig. 16). Consider the case for 1 km horizontal path links at different altitudes. This scenario may, for example, be adopted in future high data rate drone-to-drone communications. The results are shown in Fig. 17 for the four macroscopic atmospheric conditions given in Table 7. Clearly, for a 1 km path link at sea level, transmittance is almost zero from 0.75 to 1 THz (as also seen previously between 1 and *ca.* 22 THz), fundamentally limiting this part of the frequency spectrum for wireless exploitation over long distances.

From the inset of Fig. 17, extreme broadening of the 0.917 THz gaseous water vapor line is evident; at a small frequency offset from line center, transmittance decreases from 100% to almost zero, as geopotential attitude decreases from 47.64 km′ to sea level.

C. EARTH-SPACE PATH LINK CARRIER-TO-NOISE ANALYSIS

Continuing with the arbitrary scenario depicted in Fig. 12, if a continuous wave (e.g., a pilot tone) is transmitted over a free-space link at the same frequency as a molecular resonance line, the received carrier (coherent signal) power will decrease due to molecular absorption and the received noise (incoherent signal) power will increase due to molecular emission; both mechanisms contribute separately in reducing the carrier-to-noise power ratio (C/N) at the receiver.

To investigate this further, a number of simplifying assumptions will be made: (i) unless otherwise stated, the receiver is 'noiseless' and represents a complete idealized ground station (i.e., the receiver, antenna and associated interconnect feed line are all ideal); (ii) the antenna has a highly directional pencil-beam radiation pattern; (iii) Earth's atmosphere is represented by a single homogenous layer in thermodynamic equilibrium; (iv) a 'plane atmosphere' approximation is adopted (which is usually acceptable for zenith angles below 65°) [95], whereby the Earth is assumed flat with a horizontally stratified time-invariant atmosphere [96]; (v) molecular scattering is neglected with pristine conditions; (vi) Rayleigh-Jeans law can be used to approximate Planck's laws for calculating spectral radiance; and (vii) the total opacity of the atmosphere is assumed to be frequency independent. A justification of these assumptions can be found in Appendix C.

With reference to Fig. 12(b), the sky brightness temperature $T_{IN\theta}(f)$ for all source contributions (representing the effective input noise temperature to a receiver), due to molecular absorption/emission at zenith angle θ, is dependent on frequency f and given by:

$$T_{IN\theta}(f) \approx T_{CMB} \cdot e^{-\tau_\theta(f)} + T_{MAT} \cdot \left(1 - e^{-\tau_\theta(f)}\right) \quad (1)$$

Since reflectance is neglected, transmittance is $e^{-\tau_\theta(f)}$ and absorptance is $\left(1 - e^{-\tau_\theta(f)}\right)$, which is equal to the emissivity of the atmosphere in thermodynamic equilibrium. At zenith angle θ, total opacity (sometimes referred to as 'total optical path' or 'total optical thickness') $\tau_\theta(f) = \tau_0(f) \sec\theta$, where $\tau_0(f)$ is the total zenith opacity or 'total optical depth' and $\sec\theta$ is referred to as the number of air masses. $T_{CMB} = 2.725$ K is the cosmic microwave background (CMB) noise temperature and an estimate of the physical mean atmospheric temperature (known as the 'sky emission temperature' [95]) is given by $T_{MAT} = 0.95T_{AS}$.

At this point it is worth mentioning that with high zenith angles, opacity $\tau_\theta(f) \to k_\alpha(f)L$. However, with such low elevation path links, the effects of $k_\alpha(f)$ are effectively masked by the much greater path lengths through the Earth's atmosphere (with L being of the order of 8 times the 50 km′ geopotential altitude). As a result, $e^{-\tau_\theta(f)} \to 0$ and, therefore, $T_{IN\theta}(f) \sim T_{MAT}(f)$. In other words, path length, transmittance and CMB do not need to be considered when calculating the sky brightness temperature for (near-)horizontal path links.

Often, $\tau_\theta(f)$ is simply assumed to be frequency independent, which is reasonable over sufficiently narrow fractional bandwidths. Therefore, when considering the noise contribution from the Earth's atmosphere, the effective input thermal noise power to the noiseless receiver can be simply calculated from the commonly used textbook expression:

$$P_{IN} \approx kT_{IN\theta}B \quad (2)$$

where k is Boltzmann's constant and B is channel bandwidth. It should be noted that (2) is only valid for frequencies up to *ca.* 1 THz at an ambient temperature of 296 K for a 2% error. This frequency limit, the derivation of (2) and a more accurate approach for determining the input thermal noise power are discussed in Appendix C.

The carrier and noise power levels at the input to a noisy receiver C_θ and N_θ, respectively, can be expressed as:

$$C_\theta = e^{-\tau_\theta} C_{\theta V} \quad (3)$$

$$N_\theta \approx k\,(T_{IN\theta} + T_{RX})\,B \quad (4)$$

where $C_{\theta V}$ is the received carrier power within a vacuum atmosphere (i.e., without considering any molecular absorption), T_{RX} is the intrinsic noise temperature for a noisy receiver due to intrinsic noise contributions (e.g., from receiver, antenna and associated interconnect feed line). Since $e^{-\tau_\theta} \to 1$, the received noise power within a vacuum atmosphere $N_{\theta V}$ (i.e., without considering any molecular emission) is given by:

$$N_{\theta V} \approx k\,(T_{CMB} + T_{RX})\,B \sim kT_{RX}B \text{ with } T_{CMB} \ll T_{RX} \quad (5)$$

Therefore, the respective carrier-to-noise power ratios at the input to a receiver within a vacuum atmosphere $C_{\theta V}/N_{\theta V}$ and considering both molecular absorption and emission within the Earth's atmosphere C_θ/N_θ are:

$$\frac{C_{\theta V}}{N_{\theta V}} \approx \frac{C_{\theta V}}{k\,(T_{CMB} + T_{RX})\,B} \quad (6)$$

and

$$\frac{C_\theta}{N_\theta} \approx \frac{e^{-\tau_\theta} C_{\theta V}}{k\left[T_{CMB} \cdot e^{-\tau_\theta} + T_{MAT} \cdot \left(1 - e^{-\tau_\theta}\right) + T_{RX}\right]B} \quad (7)$$

Note that the spreading loss factor only affects carrier power and not the noise power. Moreover, the reduction in the receiver's input carrier power with increasing path length (having an inverse square law) is the same in vacuum as it is with a terrestrial atmosphere. Therefore, the effects of spreading loss can be ignored in this analysis. The calculated reduction in C/N at the receiver when both molecular absorption and emission are included is given by:

$$\frac{C_{\theta V}/N_{\theta V}}{C_\theta/N_\theta}(\text{dB}) \approx 10log_{10}\left\{\frac{(T_{CMB} - T_{MAT}) + (T_{MAT} + T_{RX}) \cdot e^{+\tau_\theta}}{(T_{CMB} + T_{RX})}\right\} \quad (8)$$

This is represented by Fig. 18 for different intrinsic receiver noise temperatures and atmospheric transmittance varying from 0.1 to 100% (a transmittance of zero will result in an infinite reduction in C/N for all values of T_{RX}, which cannot be displayed).

Transmittance can change significantly due to modeling errors and/or line broadening, discussed in sub-Sections A and B, respectively. With the latter, consider two channels having ultra-narrow fractional bandwidths; the first channel is located midway between two deep spectral absorption/emission lines (exhibiting high transmittance) and

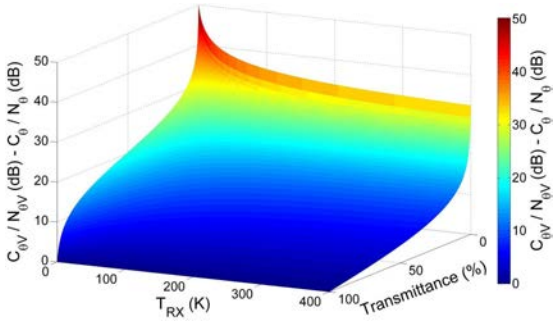

FIGURE 18. Calculated reduction in input C/N at a noisy receiver with both molecular absorption and emission considered.

the second channel is close to a spectral line (still exhibiting high transmittance). Because significant line broadening can result from changes in macroscopic atmospheric conditions, the second channel only may experience a dramatic reduction in transmittance. Therefore, this analysis can be useful for calculating the fade margins in the carrier-to-noise ratio with coherent source radiation applications below *ca.* 1 THz. For example, if the second channel experiences a drop in transmittance from 90% to 50%, with a low noise receiver having $T_{RX} = 50$ K, the fade margin (i.e., difference in the calculated reduction in C/N at the receiver) will be (8.6 – 2.3) dB = 6.3 dB; this represents a very significant proportion of the overall allocated fade margin (typically 10 dB) within a power link budget for communications applications.

It may be the case that C/N is calculated (erroneously) without considering the increase in received noise power due to molecular emission. The resulting error in C_θ/N_θ (dB) can be expressed by:

$$\frac{N_\theta}{N_{\theta V}}(\mathrm{dB}) \approx 10log_{10}\left\{\frac{T_{CMB}\cdot e^{-\tau_\theta}+T_{MAT}\cdot\left(1-e^{-\tau_\theta}\right)+T_{RX}}{T_{CMB}+T_{RX}}\right\} \quad (9)$$

The calculated error in C_θ/N_θ (dB) is shown in Fig. 19. For the limiting case of having no absorption line gives $\tau_\theta \to 0$ and $e^{-\tau_\theta} \to 1$ and $N_\theta/N_{\theta V} \to 0$ dB. However, as expected, errors are at a maximum for the opposite limiting case when both transmittance and intrinsic receiver noise temperatures values are zero. For a low noise receiver, having $T_{RX} = 50$ K, the limiting case of a strong absorption line gives $\tau_\theta \to \infty$, $e^{-\tau_\theta} \to 0$, $C_\theta \to 0$, $N_\theta \to k\,(T_{MAT}+T_{RX})\,B$, $C_\theta/N_\theta(\mathrm{dB}) \to -\infty$ and $N_\theta/N_{\theta V} \to (T_{MAT}+T_{RX})\,/\,(T_{CMB}+T_{RX}) \to 8$ dB (or $T_{MAT}/T_{CMB} \to 20$ dB with $T_{RX} \to 0$).

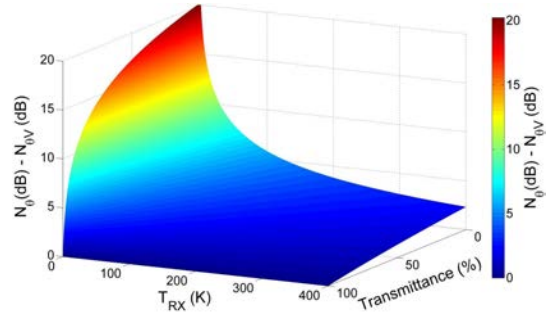

FIGURE 19. Calculated error in input C/N (dB) at a noisy receiver with only molecular absorption considered.

VII. CONCLUSION

This article tries to bridge the knowledge gap between applied engineering and atmospheric sciences, focusing specifically on atmospheric attenuation between 0.1 and 100 THz under pristine conditions (found indoors and some global location outdoors); representing a useful comparative baseline. An exhaustive review of modeling atmospheric attenuation for all outdoor weather conditions is beyond the scope of this paper, as this would require a very detailed be-spoke (time-variant or statistical) atmospheric model across every geographical path link under investigation. Nevertheless, our idealized treatment reveals many important facets associated with this multidisciplinary subject.

In practice, developing generic in-house simulation software to produce accurate predictions is challenging because of the ever-expanding spectroscopic line parameter database and improvements in radiative transfer codes. Instead, three well-known simulation software packages were employed.

The techniques used for modeling atmospheric attenuation under pristine conditions have been applied to investigate the resilience of (ultra-)wide fractional bandwidth applications to the effects of molecular absorption. Two extreme modeling scenarios were investigated: horizontal path links at sea level and Earth-space path links. It is shown by example that 'HITRAN on the Web' can give good predictions with the former (without having extensive knowledge of atmospheric science); whereas LBLRTM is recommended for the latter (requiring specialist knowledge of atmospheric science).

A 1 to 10 THz atmospheric 'band-stop' transmission characteristic is evident, even under pristine conditions, when path length extends beyond approximately 20 to 50 m at sea level. In contrast, the three transmission windows within the *'over the THz horizon'* thermal infrared represents new opportunities for exploiting this unregulated part of the electromagnetic spectrum. The recently introduced *'THz Torch'* technology represents a good candidate for investigating its resilience to molecular absorption. It is predicted that 1 km horizontal path links at sea level exhibit 90% transmittance (with Channel D).

Furthermore, in principle, if large emitting areas and narrow collimated beams are implemented, Earth-space path links can be supported, as theoretically investigated with a ground-based receiver located at Giza. However, many locations around the world can also be considered; global atmospheric reanalysis data has been compiled and used with LBLRTM to predict THz transmittance statistics. To this end, NASA's Modern Era Retrospective-analysis for Research and Applications (MERRA) dataset represents a 30 year

(1979-2007) global reanalysis, using the Goddard Earth Observing System Data Assimilation System [97].

Also, from first principles, it was shown that the Rayleigh-Jeans law approximation, widely used to calculate thermal noise power, is only valid up to *ca.* 1 THz. Moreover, 'HITRAN on the Web' predictions can be very close to estimates from the commonly used ITU-R P.676-10 model, down to *ca.* 0.56 THz. Finally, carrier-to-noise ratio fade margins have been investigated, which can take into account the effects of line broadening due to changes in molecular macroscopic atmospheric conditions for sub-1 THz ultra-narrow fractional bandwidth applications.

APPENDIX A

In this appendix, two different approaches for calculating mean channel transmittance are compared, both taking the assumption that the channel filters have a spectrally flat in-band transmittance. The first, more intuitive, definition simply uses the statistical mean:

$$T_{Channel} = \frac{1}{M} \sum_{i=1}^{M} T_i \tag{10}$$

where M is the total number of spectral data sampling points and T_i is channel transmittance for the i^{th} frequency within either the 70% or 50% transmittance channel bandwidth. This definition of mean channel transmittance is only valid if the incident power spectral density is also considered flat across the channel bandwidth.

The exact expression (adopted in this paper) for calculating mean channel transmittance takes the ratio of incident radiance at the input of a receiver to radiated radiance from a blackbody emitter and is given by:

$$T_{Channel} = \frac{\int_{f_1}^{f_2} [I_{BB}(f, T_{BB})\, T(f)] \cdot df}{\int_{f_1}^{f_2} I_{BB}(f, T_{BB}) \cdot df} \tag{11}$$

where f_1 and f_2 are the lower and upper channel cut-off frequencies, respectively; $I_{BB}(f, T_{BB})$ is the exact spectral radiance radiated from a blackbody, which is dependent on both frequency and blackbody temperature T_{BB} (878 K in our calculations, representing the nominal operating temperature for commercial thermal infrared emitters used as sources in *'THz Torch'* applications); and $T(f)$ is the frequency dependent channel transmittance.

The mean channel transmittances for each channel identified within the paper, against horizontal path length at sea level, for the two approaches (using $T(f)$ data from LBLRTM with an atmospheric temperature and pressure of 296 K and 101.325 kPa, respectively) are shown in Fig. 20. For simplicity, it is assumed that the atmosphere is homogenous at sea level.

It can be seen from Fig. 20 that the discrepancies in the results for both Channels B and D are insignificant. This is because channel transmittance is spectrally flat over their respective channel bandwidths; $T(f)$ can be moved out of the integral and, therefore, (11) equates to (10). With Channels A, C and the single channel case, transmittance is not

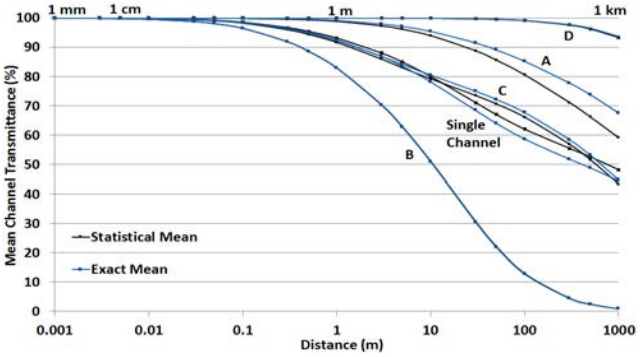

FIGURE 20. Calculated mean channel transmittance against horizontal path length at sea level for different *'THz Torch'* channels, using predictions from LBLRTM at 296 K and 101.325 kPa, (black: statistical mean; blue: exact) for $T_{BB} = 878$ K.

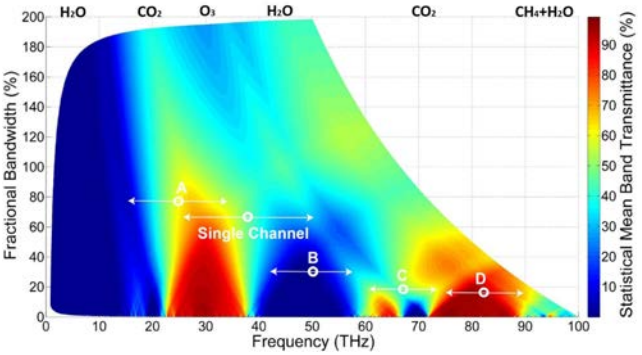

FIGURE 21. Statistical mean band transmittance against frequency and fractional bandwidth using predictions from LBLRTM for a 1 km path length.

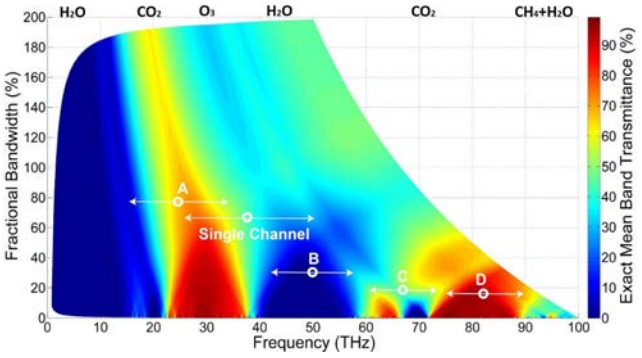

FIGURE 22. Exact mean band transmittance against frequency and fractional bandwidth using predictions from LBLRTM for a 1 km path length.

spectrally flat across their respective bandwidths. As a result, discrepancies can be seen between the statistical mean and exact expressions.

Between 0.75 and 100 THz, for a 1 km path length, the relationship between mean band transmittance, frequency and fractional bandwidth have been calculated using both definitions and the results are shown in Figs. 21 and 22, respectively. The difference in calculated mean band transmittance is shown in Fig. 23. It can be seen that this difference is less than 9% for Channel A (worst-case scenario) and much

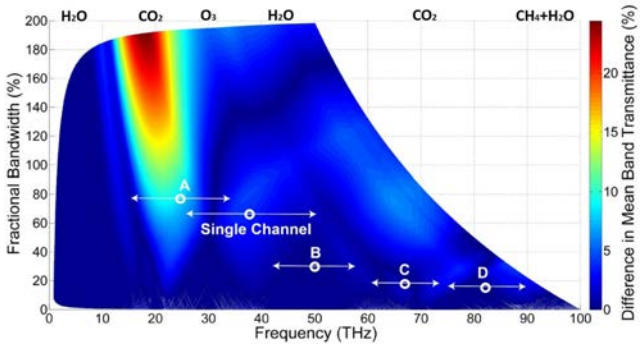

FIGURE 23. Difference between statistical and exact mean band transmittances against frequency and fractional bandwidth using predictions from LBLRTM for a 1 km path length.

lower for the other channels. Therefore, the simpler statistical mean approach can be used for some channels [54].

APPENDIX B

The linear gradient of atmospheric temperature with geopotential altitude H is referred to as the 'lapse rate'. Two equations are used for calculating barometric pressure P within the troposphere, stratosphere and mesosphere layers (up to a geopotential altitude of 84.852 km' or geometric altitude ~86 km) [53]:

$$P = P_b \cdot \begin{cases} \left[\dfrac{T_b}{T_b + L_b \cdot (H - H_b)}\right]^{\frac{g_0' M_0}{R L_b}} & \text{for } L_b \neq 0 \\ e^{-\left[\dfrac{g_0' M_0 \cdot (H - H_b)}{R T_b}\right]} & \text{for } L_b = 0 \end{cases} \tag{12}$$

where subscript b ranges from 0 to 6 (or 4 in our case; considering only the troposphere and stratosphere) in accordance with the general case of having 7 atmospheric boundaries; P_b and T_b are the barometric pressure and atmospheric temperature, respectively, corresponding to geopotential altitude H_b for the b^{th} boundary; L_b is the lapse rate of the layer above the b^{th} boundary, with our values of -6.5, 0.0, 1.0 and 2.8 K/km′, corresponding to our layers one to four having geopotential altitudes of 11, 20, 32 and 47 km′, respectively; $g_0' = 9.80665$ is the dimensional constant relating the standard geopotential meter to geometric height [53] and is numerically equal to the acceleration of gravity $g_0(\mathrm{m/s^2})$ at sea level; $M_0 = 28.9644$ kg/kmol is the mean molecular weight of air at sea level; $R = 8.31432 \times 10^3$ N·m/(kmol·K) is the gas constant. The respective reference-level values for T_0 and P_0 are 296 K and 101.325 kPa, respectively. Here, T_b with $b \in [1..4]$ is calculated from $T_b = T_{b-1} + L_{b-1} \cdot (H_b - H_{b-1})$ and P_b is obtained from (12).

APPENDIX C

In this Appendix the input thermal noise power to a noiseless receiver is derived and the condition is shown for when commonly used textbook approximations become invalid at terahertz frequencies. It is assumed throughout that 'noiseless receiver' refers to a complete idealized ground station (i.e., the receiver, antenna and associated interconnect feed line are all ideal) for Earth-space path links (as depicted in Fig. 12).

Downward spectral radiance, incident at any point on the ground, consists of contributions from: (i) CMB radiance; (ii) radiance scattered into the direction of view; and (iii) emission from the overlying bulk atmosphere. These contributions are transmitted directly into the main lobe(s) and any side lobes of the receiving antenna. Under pristine conditions, the contribution of molecular scattering can be neglected. Therefore, only atmospheric absorption and emission are considered further.

A. MULTI-LAYER ATMOSPHERE ANALYSIS

From the Beer-Lambert law, the spectral radiance absorbed by an atmospheric layer of thickness dz, $dI_a(f)$ is:

$$dI_a(f) = -I_t(f)\,\mu(f)\,\rho \sec\theta\, dz \tag{13}$$

where $I_t(f)$ is the combined spectral radiance incident at the top of the atmospheric layer and is a function of frequency, $\mu(f)$ is the mass absorption coefficient (since no scattering is assumed), ρ is the mass density of the atmospheric layer and θ is the zenith angle (from vertical to the antenna's main lobe, as shown in Fig. 12).

The amount of spectral radiance emitted by the atmospheric layer in the same direction, $dI_E(f)$ is:

$$dI_E(f) = I_{atm}(f)\,\mu(f)\,\rho \sec\theta\, dz \tag{14}$$

where $I_{atm}(f)$ is the atmospheric source term. If the atmospheric layer is in thermodynamic equilibrium, $I_{atm}(f)$ is defined by Planck's law as $I_{BB}(f, T(z))$; the blackbody spectral radiance of the atmospheric layer is a function of frequency and its physical temperature $T(z)$, with $T(z)$ itself being a function of altitude z (from the top of our defined atmosphere, as shown in Fig. 12).

In the absence of any scattering, the rate of net change in spectral radiance as a function of altitude is thus:

$$dI(f) = -\left[I_t(f) - I_{BB}(f, T(z))\right] d\tau_\theta(f) \tag{15}$$

where $d\tau_\theta(f) = d\tau_o(f) \sec\theta$ and $d\tau_o(f) = \mu(f)\,\rho\, dz$ are the optical path at θ and optical depth at zenith, respectively, over geometrical thickness dz. At θ, the total opacity of the atmosphere is $\tau_\theta(f) = \tau_o(f) \sec\theta$, where $\tau_0(f)$ is the total zenith opacity or 'total optical depth', $\sec\theta$ is referred to as the number of air masses [98], for $\theta \lesssim 65°$ [95]. From (15), using $e^{-\tau_\theta(f)}$ as an integrating factor over height, Schwarzchild's equation is obtained for the total spectral radiance $I(f, T, Z)$; describing radiative transfer in a non-scattering medium (suitable over the extended THz spectrum) as:

$$I(f, T, Z) = I_{TOA}(f, T_{CMB}) \cdot e^{-\tau_\theta(f)} + \int_0^{\tau_\theta(f)} I_{BB}(f, T(z)) \cdot \left(e^{[\tau_\theta'(f,z) - \tau_\theta(f)]}\right) d\tau'_\theta(f, z) \tag{16}$$

where Z is the surface altitude of the receiver (at sea level in our case) and $e^{-\tau_\theta(f)}$ is the atmospheric transmittance at θ, (alternatively, $e^{+\tau_\theta(f)}$ is sometimes used and referred to as the atmospheric loss factor [96], [98], as shown in Fig. 12). Total opacity $\tau_\theta(f)$ [Np] is sometimes referred to as the total optical path or thickness; $\tau'_\theta(f, z)$ is the opacity from the TOA down to altitude z. Physically, (16) shows that the downwelling spectral radiance at the receiver is comprised of the CMB radiation transmitted from the TOA plus the emission from each atmospheric layer that makes it to the surface. The CMB spectral radiance incident at the top of atmosphere $I_{TOA}(f, T_{CMB})$ is a function of frequency and CMB noise temperature T_{CMB}.

The input thermal noise power to a noiseless receiver can be most accurately expressed in terms of total spectral radiance:

$$P_{IN} = A_r \iint I(f, T)\, df\, d\Omega \tag{17}$$

where A_r is the effective radiating area for a generic radiator and assumed here to be equivalent in value for all contributions in (17).

B. SINGLE LAYER ATMOSPHERE APPROXIMATION

In order to perform basic calculations, it is often assumed that the atmosphere is represented by a single homogenous layer in thermodynamic equilibrium [95], [98]. Therefore, in (16), $T(z)$ is approximated by a single physical mean atmospheric temperature $T_{MAT} = 0.95\, T_{AS}$ (known as the 'sky emission temperature' [95]); dependent on frequency and macroscopic atmospheric conditions and can be represented with better accuracy by more sophisticated atmospheric models [99]. With this single layer assumption, the approximate total spectral radiance at the input of a noiseless receiver is:

$$I(f, T) \cong I_{top}(f, T_{CMB}) \cdot e^{-\tau_\theta(f)} + I_{BB}(f, T_{MAT}) \cdot \left(1 - e^{-\tau_\theta(f)}\right) \tag{18}$$

The first term on the right-hand side of (18) is the extraterrestrial contribution to the noiseless receiver, due to CMB radiation having a mean blackbody noise temperature of $T_{CMB} = 2.725$ K [98], [100], [101] (or more precisely 2.7255 ± 0.0009 K when measured over the spectral range from 60 to 625 GHz [102]). The second term is the terrestrial contribution, where $(1 - e^{-\tau_\theta(f)})$ is the frequency dependent emissivity of the bulk atmospheric layer. Since reflectance is neglected, absorptance is equal to the emissivity of the bulk atmospheric layer in thermodynamic equilibrium.

The approximated thermal noise power input to a noiseless receiver can now be expressed using (17), giving:

$$P_{IN} \cong A_{r1} \iint I_{top}(f, T_{CMB}) \cdot e^{-\tau_\theta(f)} df d\Omega + A_{r2} \iint I_{BB}(f, T_{MAT}) \cdot \left(1 - e^{-\tau_\theta(f)}\right) df d\Omega \tag{19}$$

where A_{r1} and A_{r2} are effective radiating areas associated with CMB radiation and bulk atmosphere, respectively. However, in practice, it can be difficult to calculate the input thermal noise power using (19), since A_{r1} and A_{r2} are unknown.

The exact spectral radiance from a blackbody $I_{BB}(f, T)$ describes the amount of energy it emits as a function of both frequency and physical temperature T, given by Planck's law:

$$I_{BB}(f, T) = \frac{2hf^3}{c^2} \frac{1}{e^{hf/kT} - 1} \tag{20}$$

where h is Planck's constant, c is the speed of light in vacuum and k is Boltzmann's constant. In the limits of high temperatures and/or low frequencies, the exponent in the exponential term becomes small and so the Taylor's first-order polynomial approximation can be used:

$$e^{hf/kT} \approx 1 + \frac{hf}{kT} \tag{21}$$

Substituting (21) into (20) gives the Rayleigh-Jeans law:

$$I_{BB}(f, T) \approx \frac{2f^2 kT}{c^2} \tag{22}$$

Using (22), the spectral radiance of any emitter $I(f, T) = \varepsilon(f, T) \cdot I_{BB}(f, T)$ can be expressed as:

$$I(f, T) \approx \frac{2f^2 kT_b(f)}{c^2} = \varepsilon(f, T) \cdot \frac{2f^2 kT}{c^2} \tag{23}$$

where the brightness temperature of the emitter $T_b(f) = \varepsilon(f, T) \cdot T$ is directly related to the physical temperature T of a blackbody in thermodynamic equilibrium by its emissivity $\varepsilon(f, T)$. Therefore, Rayleigh-Jeans law allows (18) to be greatly simplified, such that the total spectral radiance at the input of a noiseless receiver is given by:

$$\frac{2f^2 kT_{IN\theta}(f)}{c^2} \approx \frac{2f^2 kT_{CMB}}{c^2} \cdot e^{-\tau_\theta(f)} + \frac{2f^2 kT_{MAT}}{c^2} \cdot \left(1 - e^{-\tau_\theta(f)}\right) \tag{24}$$

where $T_{IN\theta}(f)$ is the sky brightness temperature for all source contributions [101], [103] (representing the effective input noise temperature for a noiseless receiver) due to molecular absorption/emission. Note that, in this case, 'effective' temperature corresponds to the temperature for a single blackbody that emits the same total amount of radiation from all source contributions. It is then a trivial matter to replace (24) by the commonly used expression [95], [99], [101], [104]:

$$T_{IN\theta}(f) \approx T_{CMB} \cdot e^{-\tau_\theta(f)} + T_{MAT} \cdot \left(1 - e^{-\tau_\theta(f)}\right) \tag{25}$$

In some textbooks, $T_{IN\theta}(f)$ is also referred to as the 'sky noise temperature' [86], [98], [100], (which should not be confused with 'sky emission temperature'). The more generic term of 'antenna noise temperature' [86], [100], [103], represents the convolution of the antenna's radiation pattern (with contributions from main and side lobes) and brightness temperature from all incoming sources (e.g., sky, objects and ground) [103]. With highly directional pencil-beam antennas

(e.g., high efficiency horn and parabolic reflectors) traditionally used in high-end applications (e.g., telecommunications, radar and radio astronomy), antenna noise temperature equates to the sky brightness temperature encompassed by the main lobe [102].

Both [86] and [103] generally ignore the first term in (25), and other extraterrestrial sources, as the contribution from CMB radiation is considered insignificant for many applications (such as low elevation path links).

The frequency dependency in (25) can be removed by averaging over the channel bandwidth $B = (f_2 - f_1)$, to give the effective input noise temperature for a noiseless receiver:

$$\overline{T_{IN\theta}} = \frac{1}{B}\int_{f_1}^{f_2} T_{IN\theta}(f)\,df = \overline{T_{CMB}} + \overline{T_{ATM}} \tag{26}$$

where f_1 and f_2 are the lower and upper channel cut-off frequencies, respectively, $\overline{T_{CMB}} = \frac{T_{CMB}}{B}\int_{f_1}^{f_2} e^{-\tau_\theta(f)}df$ is the channel's effective CMB noise temperature and $\overline{T_{ATM}} = \frac{T_{MAT}}{B}\int_{f_1}^{f_2}(1 - e^{-\tau_\theta(f)})df$ is the channel's effective atmospheric noise temperature.

Often, $\tau_\theta(f)$ is simply assumed to be frequency independent, which is reasonable over sufficiently narrow fractional bandwidths. In this case, (25) is simplified to give the following textbook representation (using a frequency invariant value for total opacity) [96], [99], [100]:

$$T_{IN\theta} \approx T_{CMB}\cdot e^{-\tau_\theta} + T_{MAT}\cdot\left(1 - e^{-\tau_\theta}\right) \tag{27}$$

As an example, with microwave Earth-space path links, atmospheric transmittance is typically ~90% and, therefore, the sky brightness temperature $T_{IN\theta}$ is ~31 K [86]; with CMB radiation contributing only 8%.

The effective thermal noise power input to a noiseless receiver can now be easily calculated from the commonly used textbook expression [86], [105], [106]:

$$P_{IN} \approx kT_{IN\theta}B \tag{28}$$

In practice, treating total opacity as being frequency independent can be a poor assumption and so (27) should be avoided with (ultra-)wide fractional bandwidth applications. Moreover, (21) to (28) are derived for the condition(s) that the temperature of a radiator is high and/or frequency is low (Rayleigh-Jeans law). It will be seen that significant errors will be introduced above *ca.* 1 THz for a range of mean atmospheric temperatures. This is illustrated by example, where the error between the left- and right-hand sides of (21) are calculated; the results are shown in Figs. 24 and 25. It can be seen that, for a 2% error, the maximum acceptable frequency is 1.3 THz at $T_{MAT} = 296$ K. Therefore, above *ca.* 1 THz, the approximate method for calculating the effective thermal noise power input to a noiseless receiver, using (28), should be replaced by (19) with a single layer atmosphere approximation.

A recent study by Jornet and Akyildiz [34] used radiative transfer theory for calculating a receiver's equivalent input noise temperature (which includes the atmospheric contribution from molecular emission), with horizontal path lengths of up to 10 m at sea level and $T_{MAT} = 296$ K. They then used the integral form of (28) to calculate the corresponding noise power, reported simulation results up to 10 THz. Using Fig. 24, it is evident that this would result in a worst-case error of 48%.

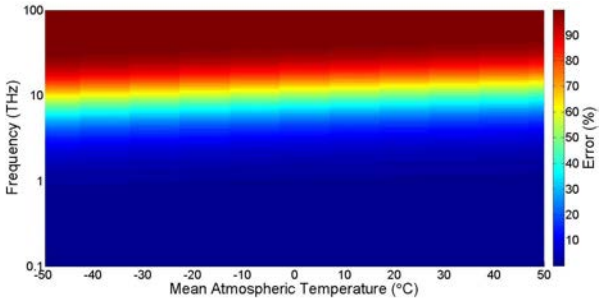

FIGURE 24. Percentage error for the Rayleigh-Jeans law approximation.

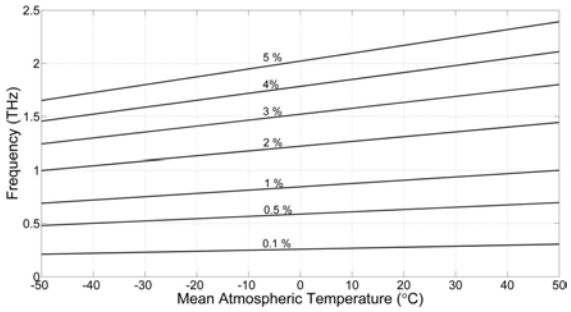

FIGURE 25. Upper frequency limits for the Rayleigh-Jeans law approximation for different levels of acceptable percentage error.

In general, however, the commonly made assumption that the atmosphere can be represented by a single homogenous layer in thermodynamic equilibrium is over-simplified. While overall transmittance $e^{-\tau_\theta}$ is the net contribution from many simulated layers, the associated temperature for each layer is fixed to just a single value of T_{MAT} within the single layer approximation. In contrast, by observing a realistic variation of atmospheric temperature, atmospheric temperature can vary significantly (from 203 to 296 K, seen in Fig. 13). For this reason, only (17) can truly determine the accurate effective thermal noise power input to a noiseless receiver.

ACKNOWLEDGMENTS

The authors wish to thank Dr. Helen E. Brindley (Space and Atmospheric Physics Group, Department of Physics, Imperial College London) for generating the MODTRAN®4 and LBLRTM data and useful discussions.

REFERENCES

[1] D. J. Hayton *et al.*, "A 4.7 THz heterodyne receiver for a balloon borne telescope," *Proc. SPIE*, vol. 9153, pp. 91531R-1–91531R-7, Jul. 2014.
[2] *Optics and Photonics—Spectral Bands*, Standard ISO 20473:2007, International Organization for Standardization, 2015.
[3] J. Harries *et al.*, "The far-infrared earth," *Rev. Geophys.*, vol. 46, no. 4, pp. 1–34, Dec. 2008.

[4] A. Mehta, *Introduction to the Electromagnetic Spectrum and Spectroscopy* (Analytical Chemistry), Pharmaxchange, Aug. 2011.[Online]. Available: http://pharmaxchange.info/press/2011/08/introduction-to-the-electromagnetic-spectrum-and-spectroscopy/

[5] G. W. Petty, *A First Course in Atmospheric Radiation*. Madison, WI, USA: Sundog Publishing, Mar. 2006.

[6] R. Appleby and H. B. Wallace, "Standoff detection of weapons and contraband in the 100 GHz to 1 THz region," *IEEE Trans. Antennas Propag.*, vol. 55, no. 11, pp. 2944–2956, Nov. 2007.

[7] H. B. Wallace, "Millimeter waves: Myths and reality," presented at the SPIE Defense Secur. Symp., Orlando, FL, USA, Apr. 2006.

[8] E. S. Rosenblum, "Atmospheric absorption of 10-400 KMCPS radiations: Summary and bibliography to 1961," *Microw. J.*, vol. 4, pp.'91–96, Mar. 1961.

[9] G. D. Lukes, "Penetrability of haze, fog, clouds and precipitation by radiant energy over the spectral range 0.1 micron to 10 centimeters," Center Naval Anal., Univ. Rochester, Arlington, TX, USA, Tech. Rep. AD847658, 1968.

[10] E. Mondre, "Atmospheric effects on millimeter wave communication channels," NASA, Washington, DC, USA, Tech. Rep. N70-34446, Mar. 1970.

[11] C. H. Zufferey, "A study of rain effects on electromagnetic waves in the 1-600 GHz ranges," M.S. thesis, Dept. Elect. Eng., Univ. Colorado, Boulder, CO, USA, 1972.

[12] M. J. Rosker and H. B. Wallace, "Imaging through the atmosphere at terahertz frequencies," in *IEEE/MTT-S Int. Microw. Symp. Dig.*, Jun. 2007, pp. 773–776.

[13] H. Liebe, "MPM89—An atmospheric mm-wave propagation model," *Int. J. Infr. Millim. Waves*, vol. 10, no. 6, pp. 631–650, Jun. 1989.

[14] H. J. P. Smith, D. J. Dube, M. E. Gardner, S. A. Clough, F. X. Kneizys, and L. S. Rothman, "FASCODE—Fast atmospheric signature code (spectral transmittance and radiance)," Air Force Geophys. Lab., Hanscom AFB, MA, USA, Tech. Rep. AFGL-TR-78-0081, Jan. 1978.

[15] *LBLRTM*. accessed on Nov. 2016. [Online]. Available: http://rtweb.aer.com/lblrtm.html

[16] *MODTRAN4 User's Manual*. accessed on Nov. 2016. [Online]. Available: ftp://ftp.pmodwrc.ch/pub/Vorlesung

[17] A. Berk *et al.*, "MODTRAN4 radiative transfer modeling for atmospheric correction," *Proc. SPIE*, vol. 3756, pp. 348–353, Oct. 1999.

[18] J. A. Shaw and P. W. Nugent, "Physics principles in radiometric infrared imaging of clouds in the atmosphere," *Eur. J. Phys.*, vol. 34, no. 6, pp. S111–S121, Nov. 2013.

[19] S. Wohnsiedler *et al.*, "Simulation and experiment of terahertz stand-off detection," *Proc. SPIE*, vol. 7215, p. 72150H, Feb. 2009.

[20] Y. Yang, A. Shutler, and D. Grischkowsky, "Measurement of the transmission of the atmosphere from 0.2 to 2 THz," *Opt. Exp.*, vol. 19, no. 9, pp. 8830–8838, Apr. 2011.

[21] T. Yuan, H. Liu, J. Xu, F. Al-Douseri, Y. Hu, and X. Zhang, "Terahertz time-domain spectroscopy of atmosphere with different humidity," *Proc. SPIE*, vol. 5070, pp. 28–37, Aug. 2003.

[22] M. J. Weber, B. B. Yang, M. S. Kulie, R. Bennartz, and J. H. Booske, "Atmospheric attenuation of 400 GHz radiation due to water vapor," *IEEE Trans. THz Sci. Technol.*, vol. 2, no. 3, pp. 355–360, May 2012.

[23] H.-B. Liu, H. Zhong, N. Karpowicz, Y. Chen, and X.-C. Zhang, "Terahertz spectroscopy and imaging for defense and security applications," *Proc. IEEE*, vol. 95, no. 8, pp. 1514–1527, Aug. 2007.

[24] D. M. Slocum, E. J. Slingerland, R. H. Giles, and T. M. Goyette, "Atmospheric absorption of terahertz radiation and water vapor continuum effects," *J. Quant. Spectrosc. Radiat. Transf.*, vol. 127, pp. 49–63, Sep. 2013.

[25] R. E. Roberts, J. E. A. Selby, and L. M. Biberman, "Infrared continuum absorption by atmospheric water vapor in the 8–12-μm window," *Appl. Opt.*, vol. 15, no. 9, pp. 2085–2090, Sep. 1976.

[26] I. V. Ptashnik, T. M. Petrova, Y. N. Ponomarev, K. P. Shine, A. A. Solodov, and A. M. Solodov, "Near-infrared water vapour self-continuum at close to room temperature," *J. Quant. Spectrosc. Radiat. Transf.*, vol. 120, pp. 23–35, May 2013.

[27] M. E. Thomas, "Infrared- and millimeter-wavelength continuum absorption in the atmospheric windows: Measurements and models," *Infr. Phys.*, vol. 30, no. 2, pp. 161–174, Dec. 1990.

[28] P. D. Green, S. M. Newman, R. J. Beeby, J. E. Murray, J. C. Pickering, and J. E. Harries, "Recent advances in measurement of the water vapour continuum in the far-infrared spectral region," *Philos. Trans. A, Roy. Soc.*, vol. 370, pp. 2637–2655, Apr. 2012.

[29] T. Schneider, A. Wiatrek, S. Preußler, M. Grigat, and R.-P. Braun, "Link budget analysis for terahertz fixed wireless links," *IEEE Trans. THz Sci. Technol.*, vol. 2, no. 2, pp. 250–256, Mar. 2012.

[30] *Attenuation by Atmospheric Gases*, document ITU-R P.676-8, International Telecommunications Union Recommendation, Sep. 2009.

[31] *Attenuation Due to Clouds and Fog*, document ITU-R P.840-4, International Telecommunications Union Recommendation, Oct. 2009.

[32] *Specific Attenuation Model for Rain for Use in Prediction Methods*, document ITU-R P.838-3, International Telecommunications Union Recommendation, Sep. 2005.

[33] "The am atmospheric model, submillimeter array," Harvard-Smithsonian Center for Astrophysics, Cambridge, MA, USA, Tech. Rep. #152. [Online]. Available: https://www.cfa.harvard.edu/ spaine/am/

[34] J. M. Jornet and I. F. Akyildiz, "Channel modeling and capacity analysis for electromagnetic wireless nanonetworks in the terahertz band," *IEEE Trans. Wireless Commun.*, vol. 10, no. 10, pp. 3211–3221, Oct. 2011.

[35] R. M. Goody and Y. L. Yung, *Atmospheric Radiation: Theoretical Basis*, 2nd ed. London, U.K.: Oxford Univ. Press, 1989.

[36] L. S. Rothman *et al.*, "The HITRAN2012 molecular spectroscopic database," *J. Quant. Spectrosc. Radiat. Transf.*, vol. 130, pp. 4–50, Nov. 2013.

[37] I. F. Akyildiz, J. M. Jornet, and C. Han, "Terahertz band: Next frontier for wireless communications," *Phys. Commun. J.*, vol. 12, pp. 16–32, Sep. 2014.

[38] C. Han and I. F. Akyildiz, "Distance-aware bandwidth-adaptive resource allocation for wireless systems in the terahertz band," *IEEE Trans. THz Sci. Technol.*, vol. 6, no. 4, pp. 541–553, Jul. 2016.

[39] S. Lucyszyn and Y. Zhou, "Characterising room temperature THz metal shielding using the engineering approach," *Prog. Electromagn. Res. J.*, vol. 103, pp. 17–31, 2010.

[40] *Calculation of Molecular Spectra With the Spectral Calculator*. accessed on Nov. 2016. [Online]. Available: http://www.spectralcalc.com/info/CalculatingSpectra.pdf

[41] J. G. Cormier, J. T. Hodges, and J. R. Drummond, "Infrared water vapor continuum absorption at atmospheric temperatures," *J. Chem. Phys.*, vol. 122, no. 11, p. 114309, Mar. 2005.

[42] W. M. Elsasser, "Mean absorption and equivalent absorption coefficient of a band spectrum," *Phys. Rev.*, vol. 54, no. 2, pp. 126–129, Jul. 1938.

[43] K. Bignell, F. Saiedy, and P. A. Sheppard, "On the atmospheric infrared continuum," *J. Opt. Soc. Amer.*, vol. 53, no. 4, pp. 466–479, Apr. 1963.

[44] S. S. Penner and P. Varanasi, "Spectral absorption coefficients in the pure rotation spectrum of water vapor," *J. Quant. Spectrosc. Radiat. Transf.*, vol. 7, no. 4, pp. 687–690, Jul./Aug. 1967.

[45] P. Varanasi, S. Chou, and S. S. Penner, "Absorption coefficients for water vapor in the 600–1000 cm^{-1} region," *J. Quant. Spectrosc. Radiat. Transf.*, vol. 8, no. 8, pp. 1537–1541, Aug. 1968.

[46] S. A. Clough, F. X. Kneizys, and R. W. Davies, "Line shape and the water vapor continuum," *Atmos. Res.*, vol. 23, nos. 3–4, pp. 229–241, Oct. 1989.

[47] E. J. Mlawer, V. H. Payne, J.-L. Moncet, J. S. Delamere, M. J. Alvarado, and D. C. Tobin, "Development and recent evaluation of the MT_CKD model of continuum absorption," *Philos. Trans. Roy. Soc. A*, vol. 370, pp. 2520–2556, Apr. 2012.

[48] T. Kuhn, A. Bauer, M. Godon, S. Bühler, and K. Künzi, "Water vapor continuum: Absorption measurements at 350 GHz and model calculations," *J. Quant. Spectrosc. Radiat. Transf.*, vol. 74, no. 5, pp. 545–562, Sep. 2002.

[49] Q. Ma and R. H. Tipping, "Water vapor continuum in the millimeter spectral region," *J. Chem. Phys.*, vol. 93, no. 9, pp. 6127–6139, Nov. 1990.

[50] *Atmospheric Radiative Transfer Codes*. accessed on Nov. 2016. [Online]. Available: https://en.wikipedia.org/wiki/Atmospheric_radiative_transfer_codes

[51] J. R. Pardo, J. Cernicharo, and E. Serabyn, "Atmospheric transmission at microwaves (ATM): An improved model for millimeter/submillimeter applications," *IEEE Trans. Antennas Propag.*, vol. 49, no. 12, pp. 1683–1694, Dec. 2001.

[52] *HITRAN on the Web*. accessed on Nov. 2016. [Online]. Available: http://hitran.iao.ru/

[53] *U.S. Standard Atmosphere 1976*. accessed on Nov. 2016. [Online]. Available: http://ntrs.nasa.gov/archive/nasa/casi.ntrs.nasa.gov/19770009539.pdf

[54] F. Hu, J. Sun, H. E. Brindley, X. Liang, and S. Lucyszyn, "Systems analysis for thermal infrared 'THz torch' applications," *J. Infr., Millim., Terahertz Waves*, vol. 36, no. 5, pp. 474–495, May 2015.

[55] S. Lucyszyn, H. Lu, and F. Hu, "Ultra-low cost THz short-range wireless link," in *Proc. IEEE Int. Microw. Workshop Ser. Millim. Wave Integr. Technol.*, Sitges, Spain, Sep. 2011, pp. 49–52.

[56] F. Hu and S. Lucyszyn, "Emerging thermal infrared 'THz torch' technology for low-cost security and defence applications," in *THz and Security Applications: Detectors, Sources and Associated Electronics for THz Applications*, C. Corsi and F. Sizov, Eds. Delft, The Netherlands: Springer, Apr. 2014, ch. 13, pp. 239–275.

[57] X. Liang, F. Hu, Y. Yan, and S. Lucyszyn, "Secure thermal infrared communications using engineered blackbody radiation," *Sci. Rep.*, vol. 4, p. 5245, Jun. 2014.

[58] F. Hu and S. Lucyszyn, "Modelling miniature incandescent light bulbs for thermal infrared 'THz torch' applications," *J. Infr., Millim., Terahertz Waves*, vol. 36, no. 4, pp. 350–367, Apr. 2015.

[59] J. Sun, F. Hu, Z. Wang, and S. Lucyszyn, "Banknote characterization using a thermal infrared 'THz torch' spectrometer," in *Proc. Asia–Pacific Microw. Conf.*, Nanjing, China, Dec. 2015, pp. 1–3.

[60] F. Hu and S. Lucyszyn, "Advances in front-end enabling technologies for thermal infrared 'THz torch' wireless communications," *J. Infr., Millim., Terahertz Waves*, vol. 37, no. 9, pp. 881–893, Sep. 2016.

[61] *The HITRAN Database*. accessed on Nov. 2016. [Online]. Available: http://www.cfa.harvard.edu/hitran/

[62] H. E. Brindley and J. E. Harries, "The impact of far I.R. absorption on clear sky greenhouse forcing: Sensitivity studies at high spectral resolution," *J. Quant. Spectrosc. Radiat. Transf.*, vol. 60, no. 2, pp. 151–180, Aug. 1998.

[63] *Software: MODTRANő Atmospheric Radiation Transport Model*. accessed on Nov. 2016. [Online]. Available: http://www.spectral.com/MODTRAN.shtml

[64] A. Berk, P. Conforti, R. Kennett, T. Perkins, F. Hawes, and J. van den Bosch, "MODTRAN6: A major upgrade of the MODTRAN radiative transfer code," *Proc. SPIE*, vol. 9088, pp. 90880H-1–90880H-7, Jun. 2014.

[65] S. B. Carr, "The aerosol models in MODTRAN?: Incorporating selected measurements from Northern Australia," Defence Sci. Technol. Organization Edinburgh (Australia), Intell. Surveillance Reconnaissance Division, Edinburgh, Australia, Tech. Rep. DSTO-TR-1803, Dec. 2005.

[66] S. A. Clough *et al.*, "Atmospheric radiative transfer modeling: A summary of the AER codes," *J. Quant. Spectrosc. Radiat. Transf.*, vol. 91, no. 2, pp. 233–244, Mar. 2005.

[67] M. J. Alvarado *et al.*, "Performance of the line-by-line radiative transfer model (LBLRTM) for temperature, water vapor, and trace gas retrievals: Recent updates evaluated with IASI case studies," *Atmos. Chem. Phys.*, vol. 13, pp. 6687–6711, Jul. 2013.

[68] M. W. Shephard, S. A. Clough, V. H. Payne, W. L. Smith, S. Kireev, and K. E. Cady-Pereira, "Performance of the line-by-line radiative transfer model (LBLRTM) for temperature and species retrievals: IASI case studies from JAIVEx," *Atmos. Chem. Phys.*, vol. 9, pp. 7397–7417, Oct. 2009.

[69] A. G. Davies, A. D. Burnett, W. Fan, E. H. Linfield, and J. E. Cunningham, "Terahertz spectroscopy of explosives and drugs," *Mater. Today*, vol. 11, no. 3, pp. 18–26, Mar. 2008.

[70] M. R. Leahy-Hoppa, M. J. Fitch, X. Zheng, L. M. Hayden, and R. Osiander, "Wideband terahertz spectroscopy of explosives," *Chem. Phys. Lett.*, vol. 434, nos. 4–6, pp. 227–230, Feb. 2007.

[71] I. Hosako *et al.*, "At the dawn of a new era in terahertz technology," *Proc. IEEE*, vol. 95, no. 8, pp. 1611–1623, Aug. 2007.

[72] B. Stuart, "Instrumentation," in *Modern Infrared Spectroscopy*. West Sussex, U.K.: Wiley, 1996, pp. 19–31.

[73] P. H. Siegel, "THz Instruments for Space," *IEEE Trans. Antennas Propag.*, vol. 55, no. 11, pp. 2957–2965, Nov. 2007.

[74] J. W. Waters *et al.*, "The earth observing system microwave limb sounder (EOS MLS) on the aura satellite," *IEEE Trans. Geosci. Remote Sens.*, vol. 44, no. 5, pp. 1075–1092, May 2006.

[75] P. H. Siegel *et al.*, "Heterodyne radiometer development for the earth observing system microwave limb sounder," *Proc. SPIE*, vol. 1874, pp. 124–137, Jul. 1993.

[76] B. B. Lahiri, S. Bagavathiappan, T. Jayakumar, and J. Philip, "Medical applications of infrared thermography: A review," *Infr. Phys. Technol.*, vol. 55, no. 4, pp. 221–235, Jul. 2012.

[77] R. Corkish, M. A. Green, and T. Puzzer, "Solar energy collection by antennas," *Solar Energy*, vol. 73, no. 6, pp. 395–401, Dec. 2002.

[78] S. Kono, M. Tani, P. Gu, and K. Sakai, "Detection of up to 20 THz with a low-temperature-grown GaAs photoconductive antenna gated with 15 fs light pulses," *Appl. Phys. Lett.*, vol. 77, no. 25, pp. 4104–4106, Dec. 2000.

[79] S. Kono, M. Tani, and K. Sakai, "Ultrabroadband photoconductive detection: Comparison with free-space electro-optic sampling," *Appl. Phys. Lett.*, vol. 79, no. 7, pp. 898–900, Oct. 2001.

[80] S. Kono, M. Tani, and K. Sakai, "Coherent detection of mid-infrared radiation up to 60 THz with an LT-GaAs photoconductive antenna," *IEE Proc.-Optoelectron.*, vol. 149, no. 3, pp. 105–109, Jun. 2002.

[81] H. Shimosato, S. Saito, M. Ashida, T. Itoh, and K. Sakai, "Ultrabroadband detection of terahertz radiation from 0.1 to 100 THz with photoconductive antenna," in *Ultrafast Optics V* (Springer Series in Optical Sciences). New York, NY, USA: Springer, Jul. 2007, pp. 317–323.

[82] J. C. Haartsen, A. Meijerink, A. Bekkaoui, A. Taban, and J. L. Tauritz, "Novel wireless modulation technique based on noise," in *Proc. IEEE Symp. Commun. Veh. Technol. (SCVT)*, Nov. 2004, p. 8.

[83] T. Thayaparan and C. Wernik, "Noise radar technology basics," Defence Res. Develop. Canada, Ottawa, ON, Canada, Tech. Rep. TM 2006-266, Dec. 2006.

[84] S. C. Surender and R. M. Narayanan, "UWB noise-OFDM netted radar: Physical layer design and analysis," *IEEE Trans. Aerosp. Electron. Syst.*, vol. 47, no. 2, pp. 1380–1400, Apr. 2011.

[85] *ADAPTIV-a Unique Camouflage System*. accessed on Nov. 2016. [Online]. Available: http://www.baesystems.com/en-uk/feature/adativ-cloak-of-invisibility

[86] G. Maral and M. Bousquet, "Comminication techniques," in *Satellite Communications Systems*. Great Britain, U.K.: Wiley, 1987, pp. 51–57.

[87] J. Y. Suen, M. T. Fang, and P. M. Lubin, "Global distribution of water vapor and cloud cover—Sites for high-performance THz applications," *IEEE Trans. THz Sci. Technol.*, vol. 4, no. 1, pp. 86–100, Jan. 2014.

[88] G. A. Ediss *et al.*, "ALMA North American integration center front-end test system," *J. Infr., Millim., Terahertz Waves*, vol. 31, no. 10, pp. 1182–1204, Oct. 2010.

[89] J. Y. Suen, M. T. Fang, S. P. Denny, and P. M. Lubin, "Modeling of terabit geostationary terahertz satellite links from globally dry locations," *IEEE Trans. THz Sci. Technol.*, vol. 5, no. 2, pp. 299–313, Mar. 2015.

[90] J. Y. Suen, "Terabit-per-second satellite links: A path toward ubiquitous terahertz communication," *J. Infr., Millim., Terahertz Waves*, vol. 37, no. 7, pp. 615–639, Jul. 2016.

[91] D. P. Dee *et al.*, "The ERA-Interim reanalysis: Configuration and performance of the data assimilation system," *Quart. J. Roy. Meteorol. Soc.*, vol. 137, no. 656, pp. 553–597, Apr. 2011.

[92] H. E. Brindley and J. E. Russell, "The direct cloud-free longwave radiative effect of Saharan dust as observed by the geostationary earth radiation budget (GERB) experiment, international radiation symposium (IRC/IAMAS)," *Amer. Inst. Phys.*, vol. 1100, no. 1, pp. 521–524, Mar. 2009.

[93] Y. Yao, A. J. Hoffman, and C. F. Gmachl, "Mid-infrared quantum cascade lasers," *Nature Pub. Group*, vol. 6, no. 7, pp. 432–439, Jun. 2012.

[94] *Attenuation by Atmospheric Gases*, document ITU-R P.676-10, International Telecommunications Union Recommendation, Sep. 2013.

[95] A. M. Melo *et al.*, "Determination of submillimeter atmospheric opacity at El Leoncito, Argentina Andes," *Bull. Astronomical Soc. Brazil*, vol. 23, no. 1, pp. 202–203, Aug. 2003.

[96] S. D. Slobin, M. M. Franco, and C. T. Steizried, "The 20.7- and 31.4-GHz atmospheric noise temperature measurements," Jet Propuls. Lab., Pasadena, CA, USA, Tech. Rep. 42-64, May/Jun. 1981, pp. 132–139.

[97] S. W. Berrick, D. Ostrenga, and S. Shen, "Modern era retrospective-analysis for research and applications (MERRA) data and services at the GES DISC," Amer. Geophys. Union, Washington, DC, USA, Tech. Rep. 5848, Dec. 2008.

[98] S. D. Slobin. (Sep. 2009). *Atmospheric and Environmental Effects, DSN Telecommunications Link Design Handbook*. [Online]. Available: http://deepspace.jpl.nasa.gov/dsndocs/810-005/105/105D.pdf

[99] J. W. Lamb, "SSB vs. DSB for submillimeter receivers," *ALMA Memo*, vol. 301, pp. 1–6, Apr. 2000. [Online]. Available: http://legacy.nrao.edu/alma/memos/html-emos/alma301/memo301.pdf

[100] N. K. Nikolova, "Lecture 7: Antenna noise temperature and system signal-to-noise ratio," Dept. Elect. Comput. Eng., McMaster Univ., Hamilton, ON, Canada, Tech. Rep. [Online]. Available: http://www.ece.mcmaster.ca/faculty/nikolova/antenna_dload/current_lectures/L07_Noise.pdf

[101] S. Shambayati, "Atmosphere attenuation and noise temperature at microwave frequencies," in *Low-Noise Systems in the Deep Space Network*, M. S. Reid, Ed. New York, NY, USA: Wiley, 2008, ch. 6, pp. 255–281. [Online]. Available: http://descanso.jpl.nasa.gov/monograph/series10/06_Reid_chapt+6.pdf
[102] D. J. Fixsen, E. S. Cheng, J. M. Gales, J. C. Mather, R. A. Shafer, and E. L. Wright, "The cosmic microwave background spectrum from the full COBE FIRAS data set," *Astrophys. J.*, vol. 473, no. 2, pp. 576–587, Dec. 1996.
[103] *Radio Noise*, document ITU-R P.372-10, International Telecommunications Union Recommendation, Oct. 2009.
[104] S. D. Slobin, "Microwave noise temperature and attenuation of clouds: Statistics of these effects at various sites in the United States, Alaska, and Hawaii," *Radio Sci.*, vol. 17, no. 6, pp. 1443–1454, Nov./Dec. 1982.
[105] K. L. Blackard, T. S. Rappaport, and C. W. Bostian, "Measurements and models of radio frequency impulsive noise for indoor wireless communications," *IEEE J. Sel. Areas Commun.*, vol. 11, no. 7, pp. 991–1001, Sep. 1993.
[106] R. M. Gagliardi, "The satellite channel," in *Satellite Communications*. The Netherlands, Springer, 2012, ch. 3, pp. 115–116.

JINGYE SUN was born in Changchun, China, in 1989. She received the B.Eng. degree in electronic and electrical engineering from University College London, London, U.K., in 2012, and the M.Sc. degree in electrical and electronic engineering from Imperial College London, London, U.K., in 2013.

She is currently pursuing the Ph.D. degree with Imperial College London. Her main research interests are in modeling atmospheric attenuation across the extended terahertz spectrum, thermal infrared THz Torch spectroscopy and its applications.

FANGJING HU received the B.Sc. and M.Sc. degrees from the University of Electronic Science and Technology of China in 2007 and 2010, respectively, and the Ph.D. degree from Imperial College London, U.K., in 2015, all in electronic engineering.

He is currently the Lead Researcher for the thermal infrared 'THz Torch' technology. His research interests include terahertz technologies and engineering, infrared systems, and computational electromagnetics. In 2016, he received the Eryl Cadwaladr Davies Prize for the best doctoral thesis in 2015, within the Department of Electrical and Electronic Engineering, Imperial College London.

STEPAN LUCYSZYN (M'91–SM'04–F'14) received the Ph.D. degree in electronic engineering from King's College London (University of London), London, U.K., in 1992, and the D.Sc. (Hons.) degree in millimeter-wave and terahertz electronics from Imperial College London, London, U.K., in 2010.

He was with Vega Space Systems Engineering Ltd., U.K., as a Satellite Systems Engineer for maritime and military communications where he was involved with microwave power link budget analysis for the INMARSAT satellite network.

He is a Professor of Millimeter-wave Systems and Director of the Center for Terahertz Science and Engineering, Imperial College London. He has co-authored approximately 200 papers and 12 book chapters in applied physics and electronic engineering. He serves as a Founding Member of the Steering Group for the U.K.'s EPSRC Terahertz Network. He is a member of the IEEE Technical Committee for Terahertz Technology and Applications (MTT-4).

In 2005, he became a fellow of the Institution of Electrical Engineers, U.K., and the Institute of Physics, U.K. In 2008, he became a fellow of the Electromagnetics Academy, U.S.A. He was an IEEE Distinguished Microwave Lecturer from 2010 to 2013. He is currently a European Microwave Lecturer for the European Microwave Association. He co-founded the Imperial College London spin-out company Drayson Wireless Ltd., in 2014.